

東京大学 大学院院領域創成科学研究科

基盤科学研究系物質系専攻

平成 30 年度

修士論文

Optical strain sensing for free-standing membrane energy

harvesting devices

環境発電デバイスへ向けたフリースタンディング薄膜における

ひずみの光学的計測

2019 年 1 月 22 日提出

指導教員 リップマー ミック 教授 印

小川 幸大

Contents

1	Introduction.....	3
2	Materials background.....	8
2.1	BaTiO ₃ as a piezoelectric	8
2.2	Metal-insulator transition in VO ₂	11
3	Fabrication and characterization of thin films	15
3.1	Introduction.....	15
3.2	Pulsed laser deposition.....	15
3.3	Reflection high-energy electron diffraction.....	18
3.4	Atomic Force Microscopy.....	20
3.5	X-ray diffraction.....	22
4	Freestanding film of BaTiO ₃	25
4.1	Introduction	25
4.2	Using a Ge substrate	26
4.2.1	Growing a BaTiO ₃ film on a Ge substrate.....	26
4.2.2	Etching process of a Ge substrate.....	29
4.3	Using a water-soluble layer	32
4.3.1	Fe ₃ O ₄ /BaO/SrTiO ₃	32
4.3.2	Etching process of BaO	34
4.3.3	BaTiO ₃ film on a BaO buffer layer	35
5	Sensing local strain in thin films	39
5.1	Introduction	39
5.2	Fabrication of VO ₂ thin films on TiO ₂ substrates.....	39
5.2.1	TiO ₂ substrate	39
5.2.2	Structural and electrical properties of VO ₂ films	41
5.2.3	Optical properties of VO ₂ thin films.....	48

5.3	Bending stage and measurement system	51
5.3.1	Thinner substrate for bending.....	51
5.3.2	Reference for film reflectance measurement.....	54
5.3.3	The bending stage and the measurement system	55
5.4	Strain dependent optical reflectivity of VO ₂ thin films.....	60
5.4.1	Calculation of strain value.....	60
5.4.2	Resistance measurement on the bending stage	61
5.4.3	MIT properties during sample bending.....	62
6.	Conclusion.....	66
	References	68
	Acknowledgments	71

1 Introduction

Low-power energy harvesting is a technique where energy is collected from the environment for the purpose of providing a power supply for distributed electronic applications. This technology is expected to provide a low-voltage power supply for low-power devices such as remote environmental sensors that have wireless communication capabilities but no convenient power supplies. Energy harvesting supplies can be used in cases where batteries are either too large or difficult to replace, as in implanted medical devices.

Environmental energy is available in various forms, as heat or in the form of mechanical motion. Such environmental energy sources generally have very low energy density [1], which is why such sources are generally not considered for large-scale energy conversion and the residual energy is usually released into the environment as heat or converted to heat. The energy needs of low-power sensor devices, however, are very modest and therefore even low-density energy supplies that are widely available become attractive, especially if the captured residual energy is a byproduct of the same natural environmental phenomenon or industrial process that a remote sensor is designed to monitor. Examples of such low-density energy supplies are mechanical stress and strain, thermal energy, solar energy, wind or fluid flow energy, etc.

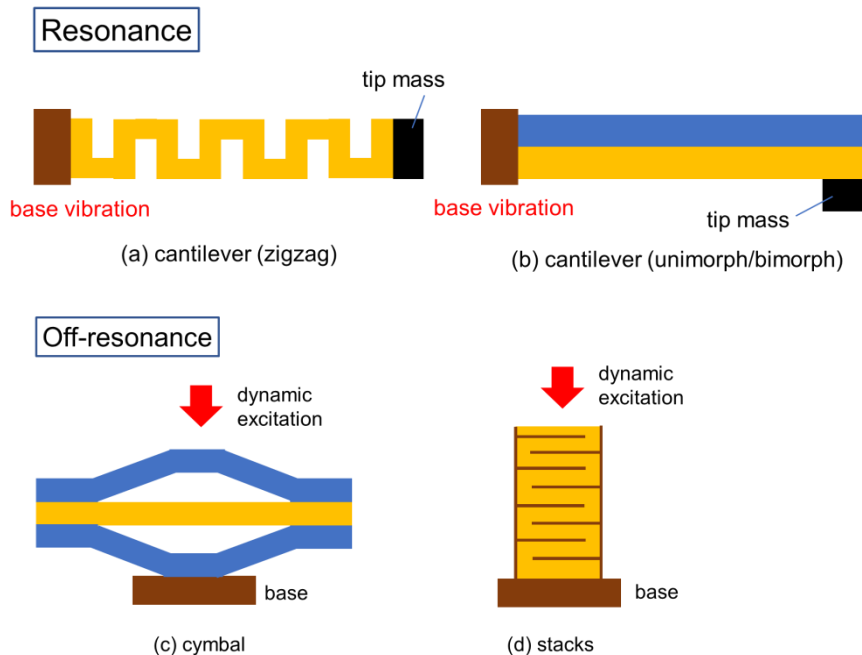


Fig. 1.1 Examples of piezoelectric energy harvester architectures.

<https://www.americanpiezo.com/blog/piezoelectric-energy-harvesting/>

This thesis work focuses on vibrational energy harvesting. This is a technique for converting low-frequency mechanical vibrational energy into an electric current. Typical applications of vibrational energy harvesting are in constructing power sources for wireless sensors for environmental parameters, such as temperature, humidity, fatigue of construction materials, or industrial processes. Vibrational energy may also be used to power personal devices, such as a wristwatch or a heart pacemaker. Specifically, my work is related to using piezoelectric thin film materials to convert mechanical vibrational energy into an electric current.

Piezoelectrics are materials that generate an electric charge when mechanical stress is applied. In this study, barium titanate (BaTiO_3) was used as a piezoelectric material. For vibrational energy conversion, dynamic strain is applied on a piezoelectric material by applying mechanical bending stress. Fig 1.1 shows examples of energy harvesting device structures that use piezoelectric materials. The cantilever geometry is often used to develop vibrational energy harvesters because a large mechanical strain can be produced in a piezoelectric thin film material and the device can be prepared by standard lithographic etching techniques. A detailed illustration and a picture of an

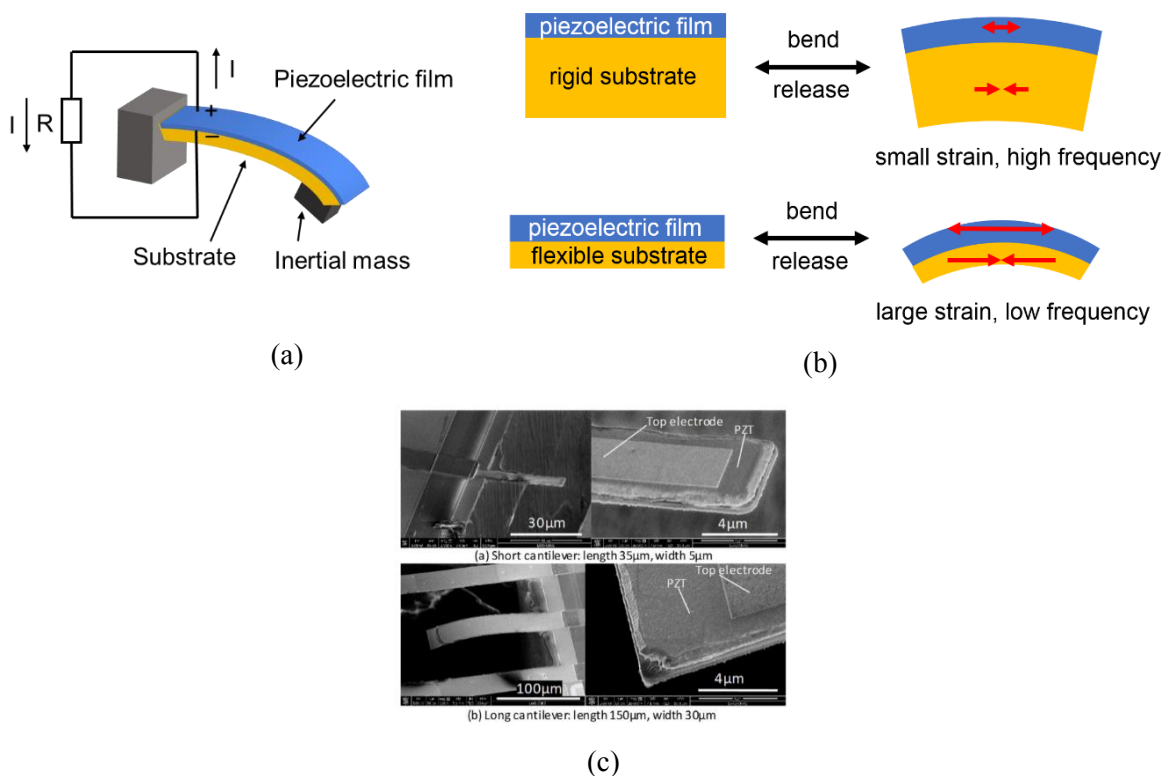


Fig. 1.2 (a) A drawing of a cantilever structure. (b) Strain comparison between a rigid substrate and a flexible substrate. (c) PZT cantilever with a 200 nm PZT film on a 300 nm Si substrate. Two electrodes are put on the top and bottom of the PZT film.

actual lead zirconate titanate (PZT) cantilever are shown in fig. 1.2. A piezoelectric thin film is grown on a substrate and the substrate is partially etched away to form the cantilever and to adjust the cantilever thickness, which also changes the spring constant and the resonant frequency of the device. A weight is attached at the end of the cantilever to apply dynamic strain on the piezoelectric film when the cantilever vibrates. If electrodes are attached to the film, an alternating current can be produced in an external circuit.

The efficiency of a piezoelectric energy converter depends on the crystal quality of the piezoelectric material. To obtain the best possible crystalline thin film, piezoelectric films are generally grown on single crystal substrates that are mechanically rigid. However, only limited strain can be applied on such ceramic piezoelectric thin films due to the presence of the rigid substrate (fig. 1.2 (b)), which means that the performance of the device is limited by the substrate, not the film itself. The resonant frequency is also an important factor when considering the energy conversion efficiency [2]. A rigid substrate has a high Young's modulus and thus also a high resonant frequency. However, much of the available vibrational energy in the environment is available at low frequencies, typically much lower than 200 Hz. The high resonance frequency of a rigid substrate is thus another reason why piezoelectric films on oxide substrates are not useful for vibrational energy harvesting from the environment.

These problems problem can be solved by constructing free-standing flexible devices where the piezoelectric film is grown on a single crystal substrate to obtain good crystallinity, and then the film is transferred from the single crystal substrate to a flexible carrier. This process has to be used because piezoelectric oxide thin films should generally be grown at high temperatures to obtain the highest piezoelectric energy conversion coefficient. Flexible substrates like a polymer sheet cannot be heated

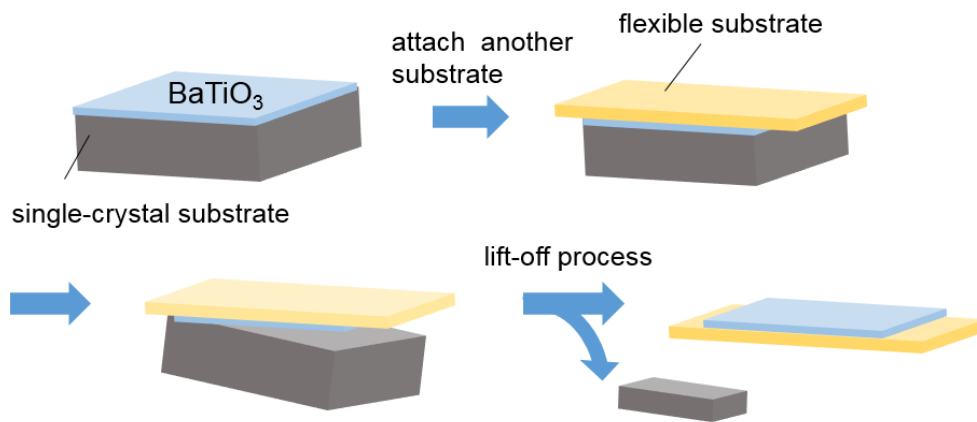


Fig. 1.3 Schematics of how to make the free-standing film structure.

to high temperatures and doesn't provide the necessary crystalline template for a crystalline film. For this reason, functional oxides cannot be grown on flexible substrate directly and a lift-off process for thin films is needed.

A schematic overview of this process is shown in fig. 1.3. At first, a BaTiO₃ thin film is deposited on a rigid substrate. After a flexible substrate has been attached to the top of the sample, the original single crystal substrate is removed and only the thin BaTiO₃ film remains on the flexible substrate.

The motivation of my study is to develop a thin film fabrication process for free-standing BaTiO₃ piezoelectric films and to analyze the strain that occurs in such devices during mechanical deformation.

Measuring the magnitude and spatial distribution of local strain is an important issue in designing an energy harvesting device. When a piezoelectric film is transferred to a flexible polymer backing it is difficult to measure how large the local strain is within the area of a millimeter-scale device structure. For very thin piezoelectric films, regions of higher or lower strain may form, resulting in fracturing the thin film. Optical analysis of the surface deformation is possible as shown in fig. 1.4 which is a calculated strain profile of cantilever from its shape [3]. However, it may not be reliable for films with large grains, where strain relaxation may occur at grain boundaries rather than by straining the bulk of each grain. Strain is inhomogeneous in each domain.

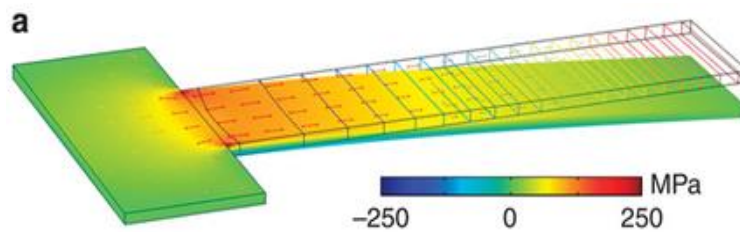


Fig. 1.4 Simulated stress profile of a cantilever device. [3]

An internal strain detector is thus needed to analyze the performance of flexible devices. One possible solution is to coat a piezoelectric film with a VO₂ layer. VO₂ has a metal-insulator transition (MIT) close to room temperature. This MIT can be induced by applied forces, like temperature, electric field, light, and dynamic strain and domain change during MIT can be measured optically by measuring the infrared reflectivity change. Fig. 1.5 shows the domain structure during MIT which is caused by temperature change [4,31].

Fig. 1.5 (a) shows the domains of a relaxed VO₂ film grown on a Al₂O₃ substrate, measured by scanning near-field infrared microscopy. In the nearly strain-free VO₂ film,

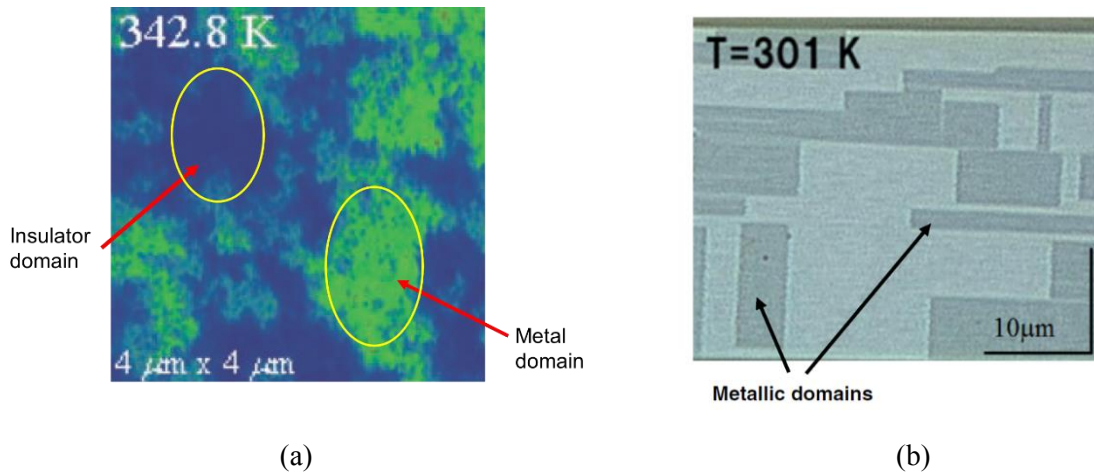


Fig. 1.5 The domains of VO₂ film on Al₂O₃ substrate by scattering scanning near-field infrared microscopy (a) and the domains of VO₂ film on TiO₂ substrate by an optical microscope (b) in the middle of MIT. [4,31]

the characteristic metallic or insulating domain size is on the order of tens of nanometers (fig. 1.5 (a)). The domain structure is strongly affected by the epitaxial strain. As shown in fig. 1.5 (b), the domains become much larger, on the scale of tens of micrometers in a highly strained VO₂ film grown on a TiO₂ substrate.

The brightness difference between the brighter insulating and darker metallic domains in the image is due to the transmittance difference between metallic and insulating domains. It is considered that this reflectance difference can be obtained during MIT which is caused by dynamic strain. The local reflectivity change of a VO₂ film can thus be used to measure the local strain distribution in a bending sample. Since the necessary thickness of the VO₂ layer is on the order of just 10 nm, the VO₂ film would not have a significant effect on the elastic properties of the much thicker piezoelectric layer. The specific purpose of this work is to obtain the reflectivity change during MIT which is caused by the bending of the sample to as a step to measure the local strain distribution.

Regardless of the domain structure, when the film surface is viewed with a simple CCD camera without a microscope, 1 pixel in the image corresponds to an area of 20 to 40 μm, which is much larger than the characteristic domain size. The local brightness seen in reflection geometry with a near-infrared camera is thus a measure of the average fraction of the film that is in the metallic state.

2 Materials background

In this study, BaTiO₃ thin films and VO₂ thin films were grown on various substrates. A brief overview of the properties of BaTiO₃ and VO₂ are presented in this chapter.

2.1 BaTiO₃ as a piezoelectric

A piezoelectric crystal, as illustrated in Fig. 2.1, exhibits spontaneous ordering of dipoles, which leads to a permanent internal electric field and opposite charges on to surfaces. When external mechanical stress is applied on a piezoelectric crystal, even a small strain causes sufficient displacement of atoms in the crystal to change the

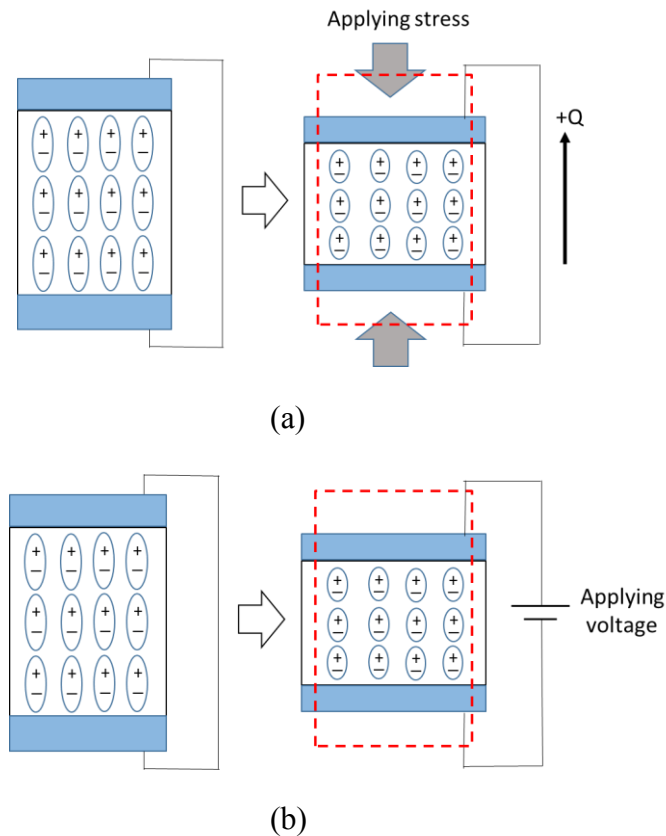


Fig. 2.1 Positive piezoelectric effect (a) and inverse piezoelectric effect (b).

macroscopic polarization, resulting in a change of the surface electric charge. This is called the positive piezoelectric effect. On the other hand, when a voltage is applied to the polar surfaces of a piezoelectric, the strain state changes. This is called the inverse piezoelectric effect (Fig. 2.1). Piezoelectric materials have been used to develop various

devices, such as SONAR, ultrasonic transducers [5], precision actuators [6,7], displacement and force sensors [8,9], etc [10].

A piezoelectric material can be used as an energy conversion device that directly converts between electric charge and mechanical displacement [11]. A piezoelectric transducer can thus be used either as a motor powered by an alternating electric current, or a generator, converting periodic mechanical movement into an electrical current. Recently, piezoelectric generator devices have been developed that use thin films instead of bulk polycrystalline ceramics. This allows microscale energy conversion in microelectromechanical systems (MEMS). Many applications of piezoelectrics use lead-based materials because of the very high strain-to-charge conversion coefficient [12]. However, the current trend in electronic materials is to reduce the burden on the environment and human health by reducing the use of heavy metals in electronic components. Development of high-performance lead-free piezoelectric materials is thus necessary to replace existing lead-based compositions [13].

In this study, barium titanate (BaTiO_3) was chosen as a lead-free piezoelectric material. Besides being piezoelectric, i.e., exhibiting a permanent spontaneous polarization, BaTiO_3 is also ferroelectric, which means that the polarization direction can be switched by an external electric field. Ferroelectrics are materials in which the dipole moment remains aligned even without an applied external electric field and the polarization direction can be changed if a sufficiently strong electric field, above the critical coercive field, is applied. All ferroelectric materials are thus piezoelectric and many ferroelectrics are actually used as piezoelectric materials.

BaTiO_3 has a cubic crystal structure at temperatures above 120 °C, the Curie temperature. In a cubic lattice, the a , b , and c axes all have the same length and the angles between any two axes is 90°. Such crystals have a center of symmetry. Below the Curie temperature, BaTiO_3 goes through a structural phase transition and becomes tetragonal with the c -axis becoming longer than the a and b axes (fig. 2.2 (a)). As shown in fig. 2.2 (b), the Ti^{4+} ion is shifted by about 0.1 Å along the c -axis, resulting in spontaneous polarization of the whole crystal. The surface towards which the Ti^{4+} ions shift obtains a positive charge the other surface gets a negative charge. When applying a force along the c -axis, the a and b -axes will become slightly longer and the c -axis shrinks. The spontaneous polarization decreases in proportion to the strain and the surface charge will be reduced accordingly, resulting in a current in an external circuit connected to the crystal. On the other hand, when removing the force, the spontaneous polarization will return to the original state and a current with the opposite polarity will flow in a circuit to compensate for the surface charge change. If this external current is

rectified, a stable power supply can be built for powering an electronic device when oscillating stress is applied on a piezoelectric material. This is the principle of a vibrational energy harvesting device.

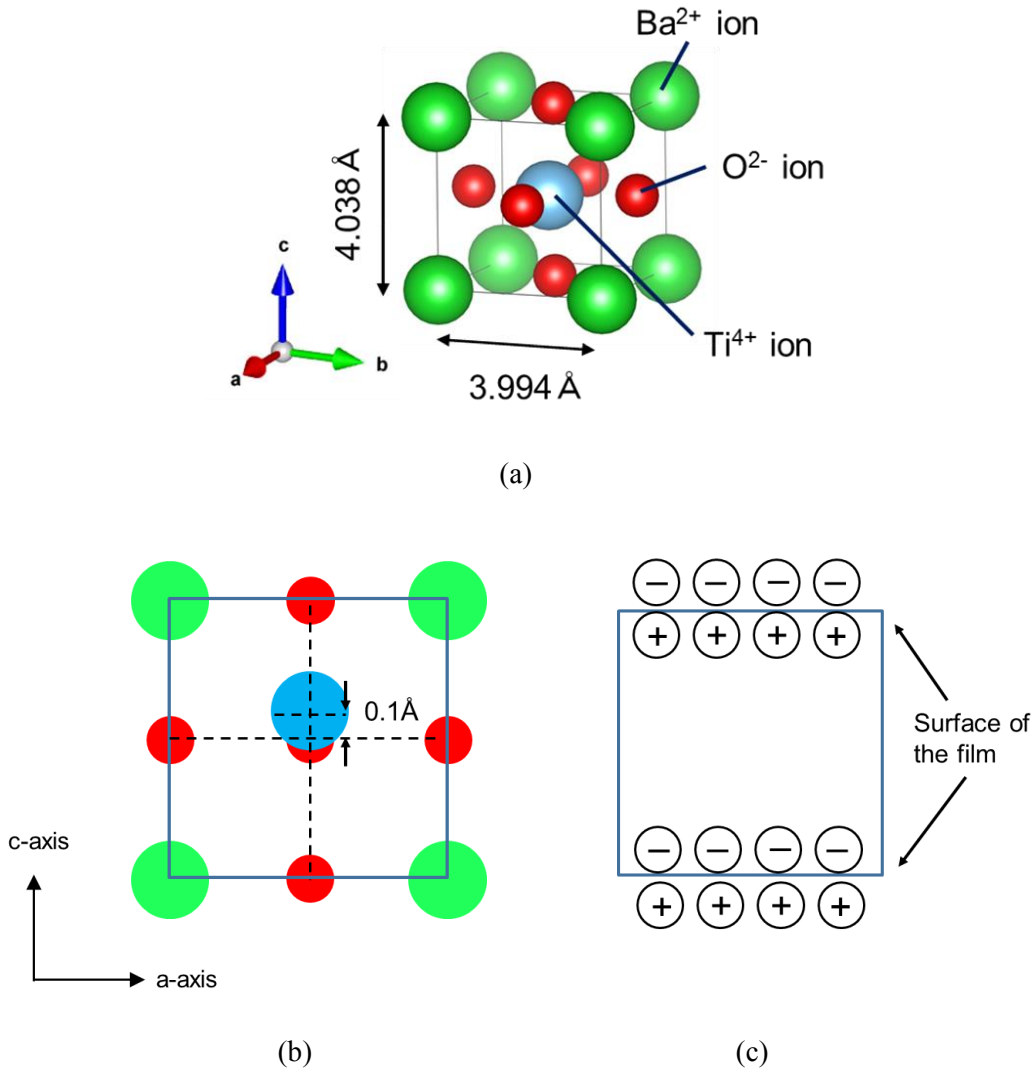


Fig. 2.2 (a) Perovskite structure of BaTiO_3 . (b) The displacement of a Ti^{4+} ion along the c -axis. (c) Schematic of electric charge arising near the surface.

2.2 Metal-insulator transition in VO₂

Stoichiometric VO₂ undergoes a metal-insulator transition (MIT) at a temperature of 340 K at ambient pressure. This MIT of bulk VO₂ is very sharp as shown in fig. 2.3(a) [14]. The significant resistance change is accompanied by a structural transition from a high-temperature rutile phase to a low-temperature monoclinic phase. The crystal structures of metallic and insulator phase are shown in fig. 2.3 (b) [15].

Although the MIT is usually considered to be a temperature-driven transition, the phase transition in VO₂ can be triggered not only by scanning the temperature [16,17], but also by applying light [18,19,20,21] or an electric-field [22], as shown in fig. 2.4.

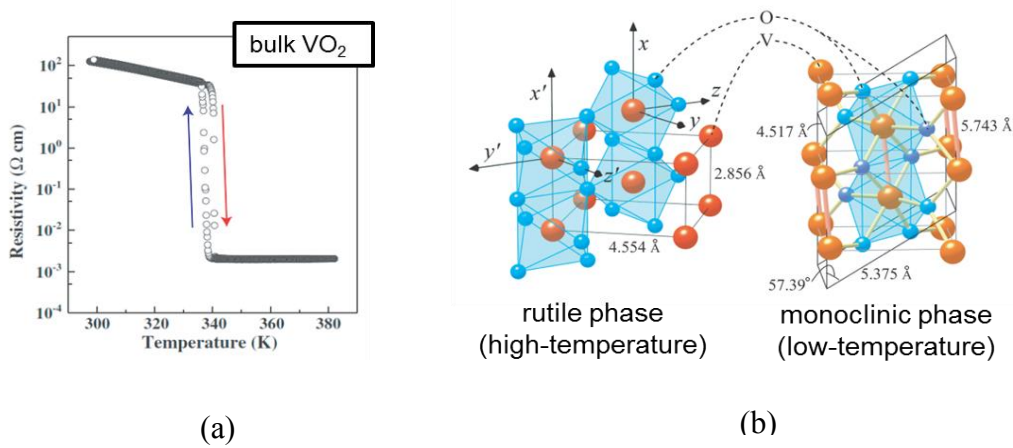


Fig. 2.3 (a) Resistance change during MIT of bulk VO₂. [14] (b) Structural change during MIT of VO₂. [15]

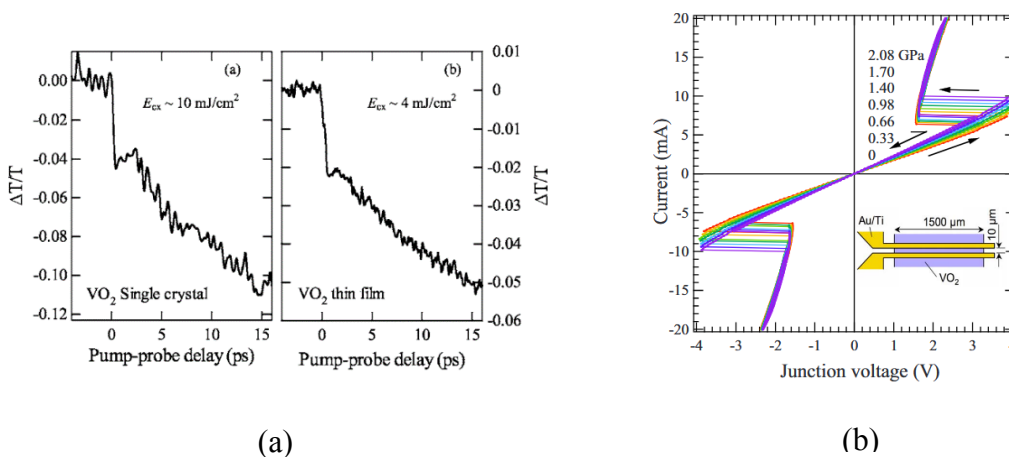


Fig. 2.4 Examples of MIT in VO₂, triggered by various external excitations: (a) light, (b) electric field. [21,22]

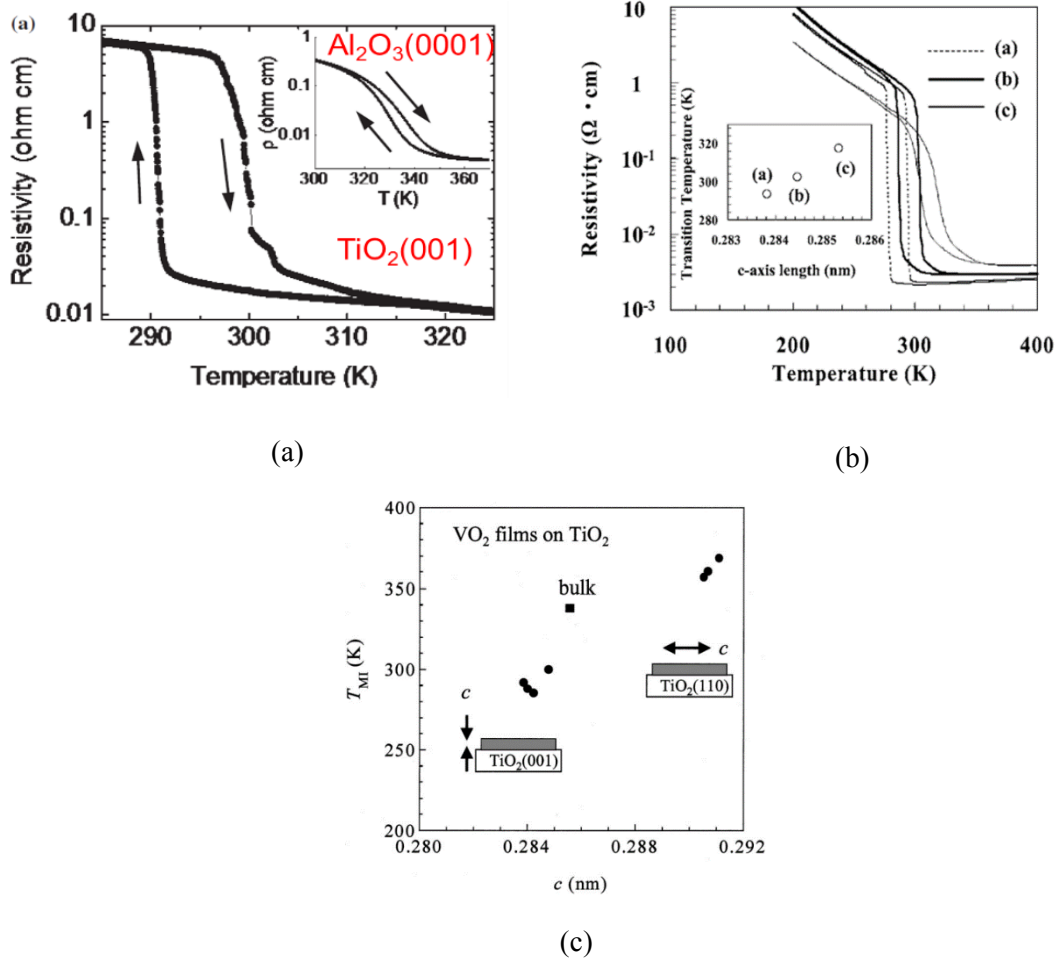


Fig. 2.5 MIT of VO₂ films (a) on different substrates and (b) on different surfaces of the same substrate material (TiO₂). (c) Transition temperature vs *c*-axis lattice parameter in VO₂ films on TiO₂ substrate. [4,23,32]

It is known that this transition is also strongly affected by other parameters, such as doping and strain. The transition temperature of VO₂, T_c , can be shifted by pressure in bulk crystals or by epitaxial strain from the substrate in thin films. Fig. 2.5 (a) shows an example of the strain effect on the MIT in VO₂ thin films grown on different substrates [4]. Since the lattice mismatch is different for films grown on TiO₂ (highly strained) and Al₂O₃ (nearly relaxed) substrates, the T_c shifts by about 50 K. Fig. 2.5 (b) shows the interface effects on the transition properties of 8 nm thick VO₂ thin films [23]. These films were grown on TiO₂ (001) substrates, but the substrates were prepared differently, having slightly different surface morphologies: mechanically polished surface (a), step-and-terrace surface (b), and a reconstructed surface (c). The inset figure shows the *c*-axis length of each film. The film grown on a mechanically polished surface has the shortest *c*-axis length, indicating that the VO₂ film was fully strained by the substrate,

while growing VO₂ on a reconstructed substrate surface led to a longer *c*-axis. Strain relaxation at the substrate interface is thus an important consideration when designing a VO₂ thin film device. There is a direct correlation between the transition temperature and the *c*-axis length. Besides the T_c shift, the fully strained sample also shows a sharper transition in addition to the lower transition temperature. On the other side, the relaxed sample having a longer *c*-axis length shows a much more gradual transition and a bulk-like transition temperature. These results show that, strong strain from the substrate is needed to get a sharp transition in VO₂ thin films and for this reason, VO₂ thin films were grown on TiO₂ (001) substrates in this study.

The effect of strain on the VO₂ film MIT temperature can be clearly seen in fig. 2.5 (c), where VO₂ films were grown on differently oriented TiO₂ substrates. Applying compressive *c*-axis strain (out of plane) leads to a large drop of the transition temperature.

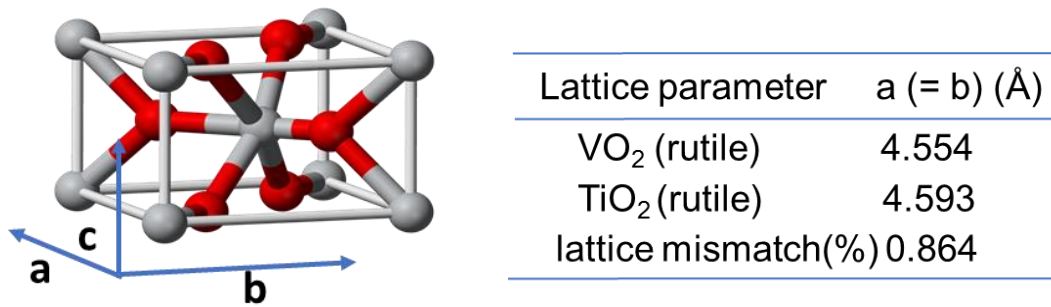


Fig. 2.6 The crystal structure and lattice parameter of the TiO₂ rutile phase.

The crystal structure of the TiO₂ rutile phase is shown in fig. 2.6. The *a* and *b* axes of the TiO₂ rutile structure are very close to the VO₂ rutile structure. Owing to this small lattice mismatch, VO₂ thin films can be expected to grow epitaxially and under strong epitaxial strain on aTiO₂ substrate. The *a* and *b* lattice parameters of VO₂ are slightly shorter than TiO₂ and an ideally strained VO₂ thin film should thus be expanded along the *a* and *b* axes and compressively strained along the *c*-axis. Thus, a fully-strained VO₂ film needs to be grown on a TiO₂ (001) substrate to obtain the shortest possible *c*-axis length.

Optical properties of a VO₂ thin film also change along with the MIT. When a VO₂ film switches from the insulating to a metallic state, the whole film does not switch at the same temperature. Instead, the switching occurs grain by grain, with some grains remaining insulating while others are metallic [24]. In the middle of the transition, as was shown in fig. 1.4, metallic domains in a VO₂ film appear darker than the insulating domains in the reflectance image of a thin film sample. This color change is related to

the absorption change due to free carriers appearing in the metallic state. Fig. 2.7 shows optical transmittance spectra of a VO₂ thin film at various temperatures around the MIT [25]. The films were grown on a SiO₂ substrate and the thickness was about 100 nm. The inset shows the temperature dependence of the transmittance at a wavelength of 1500 nm. The transmittance became lower in the metallic state at high temperature than in the insulating state at low temperature. Since most of the light in the reflectance image is scattered back from the back of the substrate, the decreasing transmittance leads to metallic domains appearing darker in a camera image of a VO₂ thin film. The transmittance drop is larger at longer wavelengths, as shown in fig. 2.7. Although longer wavelengths are convenient for detecting small differences in optical absorption, there is a wavelength limit of about 1100 nm for silicon-based CCD cameras. For this reason, measurements in this work were done at around 1000 nm.

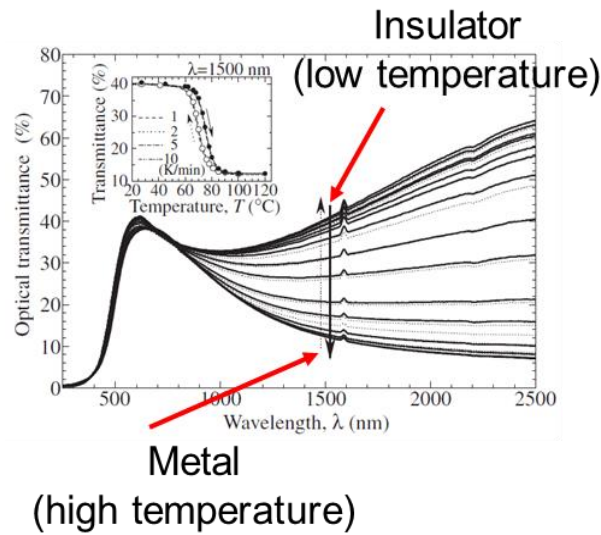


Fig. 2.7 Optical transmittance of VO₂ thin films. [25]

3 Fabrication and characterization of thin films

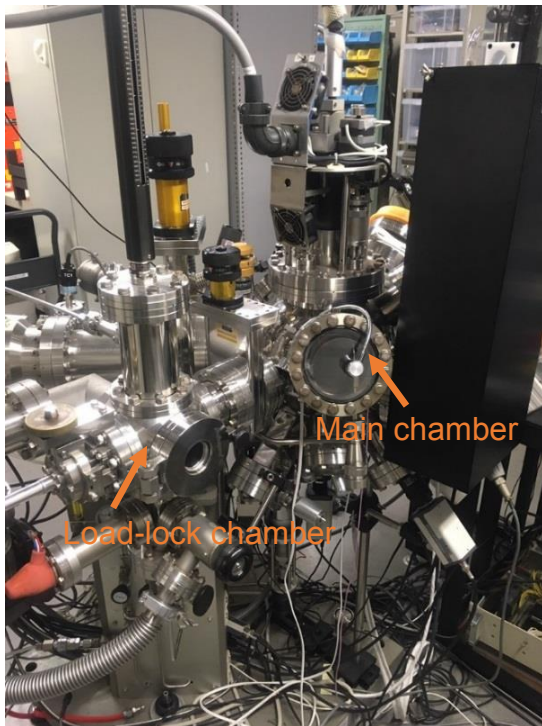
3.1 Introduction

The experimental equipment used in this study is described in this Chapter. All thin films used in this study were grown by pulsed laser deposition (PLD). The surface morphology of the films was monitored in situ by reflection high-energy electron diffraction (RHEED) and by atomic force microscopy (AFM) after unloading from the vacuum chamber.

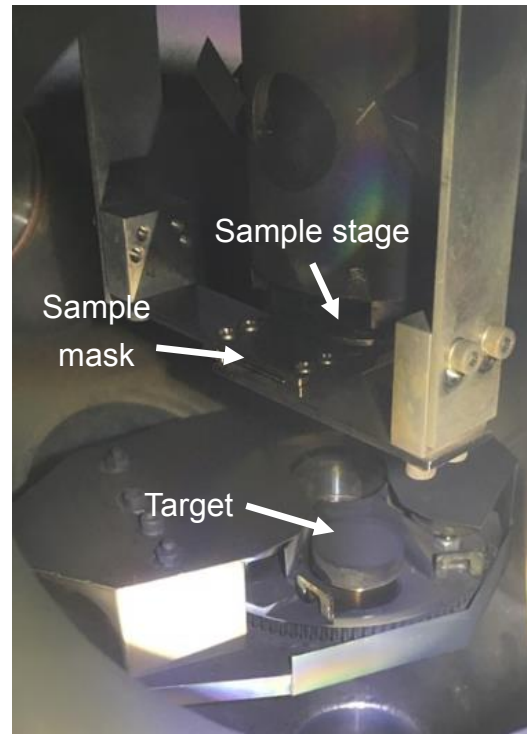
3.2 Pulsed laser deposition

Pulsed laser deposition (PLD) is a film making process where a target material is vaporized using light energy from a pulsed laser. PLD is one of the physical vapor deposition methods for thin films, besides molecular beam epitaxy and sputtering. A common feature of all these techniques is that atoms are vaporized from a target surface in vacuum or low-pressure background gas and deposited on the substrate. The main advantage of PLD over other physical vapor deposition methods is the way to supply atoms or clusters to the substrate. For example, in sputtering, particles are ejected from a target material because of the bombardment of the target by ionized particles and the ejected atoms are deposited on the substrate. In the PLD process, neutral atoms and ions are ejected by the irradiation of high intensity pulsed laser light and are deposited on the substrate surface. When the target absorbs the pulsed laser light, the rapid momentary increase of target surface temperature evaporates material from a thin surface layer of the target. If the photon energy of the laser is high enough, the light absorption is confined to a very thin surface layer and evaporation can occur without heating a large volume of the target. This is an important feature that helps to maintain stoichiometric evaporation from the target surface. The evaporated ions form a high-energy plasma plume that expands rapidly in vacuum and transports atoms or ions to the substrate.

The merit of PLD method is that nearly stoichiometric evaporation can be achieved for very high melting point materials and it is thus possible to obtain high-quality oxide thin films by using stoichiometric ceramic targets. By using RHEED during deposition, it is possible to monitor crystal growth layer by layer and to construct heterostructures with sharp interfaces. A particularly convenient feature of PLD is that it is relatively easy to prepare a target. Conventional ceramic powder synthesis can be used to make a target pellet with the desired stoichiometry or doping level. In the case of MBE, obtaining the desired film composition can be difficult because vapor pressures are different for each atomic species. In PLD such problems can usually be avoided because the laser ablation process is not dependent on atomic weight and the PLD plume composition is very close to the target composition. Another merit of PLD for oxide synthesis is that PLD can be used for thin film growth over a wide range of ambient oxygen pressures. The pressure range during the growth process can vary from the chamber base pressure of 10^{-9} Torr to 1 Torr. This is a much broader range than can be used in sputtering or MBE and very useful for obtaining the desired oxide phase.



(a)



(b)

Fig. 3.1 A photograph of the deposition chamber (a) and the inside view of the main vacuum chamber (b).

Fig. 3.1 shows a photo of the PLD chamber that was used in this work and a schematic illustration of the major components of the chamber are shown Fig. 3.2.

As an ablation laser, a Nd:YAG laser was used for making BaTiO₃ films and a KrF excimer laser for depositing VO₂ films.

Fig 3.3 shows a picture of a high-temperature sample holder on which the substrates were attached. The substrate crystals were clamped onto SiC heat spreader blocks with a stainless steel wire clamp. The SiC block was heated with a collimated infrared laser and it transferred the heat to the substrate. A platinum foil or a layer of platinum paste was used to improve the thermal contact between the substrate and the SiC block and to achieve a uniform temperature distribution of the substrate. The temperature was controlled with an optical pyrometer that measured the temperature of the SiC block and provided a feedback signal for the computer that controlled the heating laser power. The SiC block temperature is reported as the substrate temperature, assuming that the temperature difference between the substrate surface and the SiC block is insignificant.

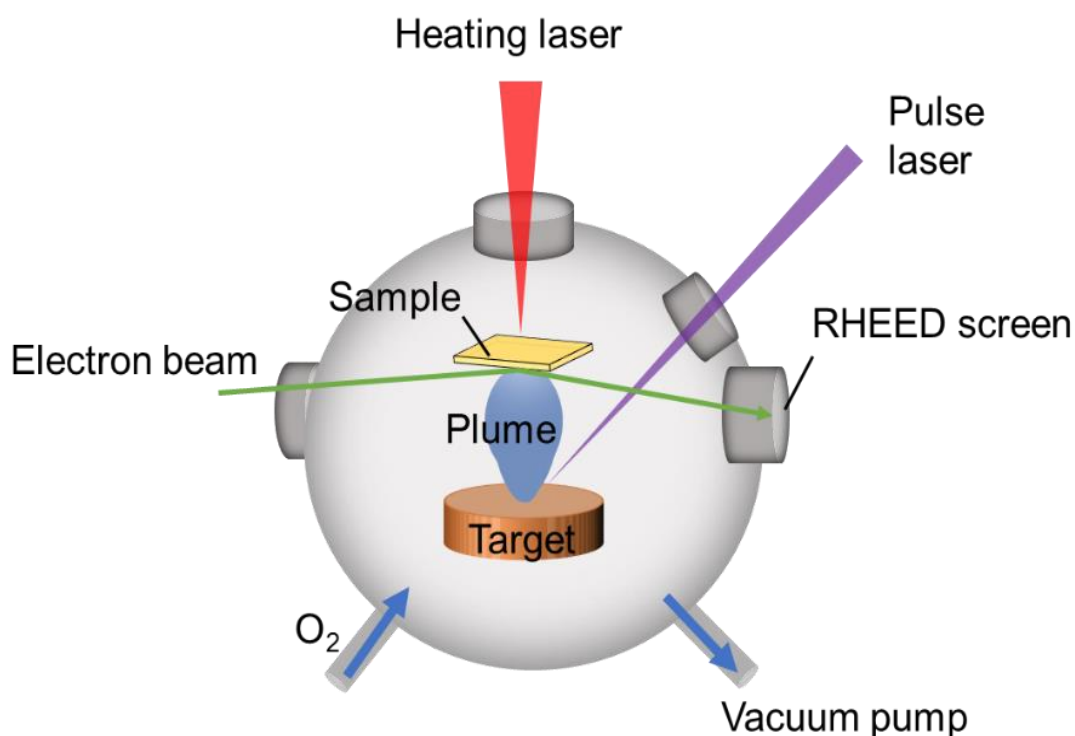


Fig. 3.2 Schematic illustration of the PLD chamber. Pulsed laser ablates the target surface, creating a plasma plume in the chamber. When ejected atoms reached the sample surface, the film grows. It is possible to monitor the surface morphology and the film growth rate by RHEED.

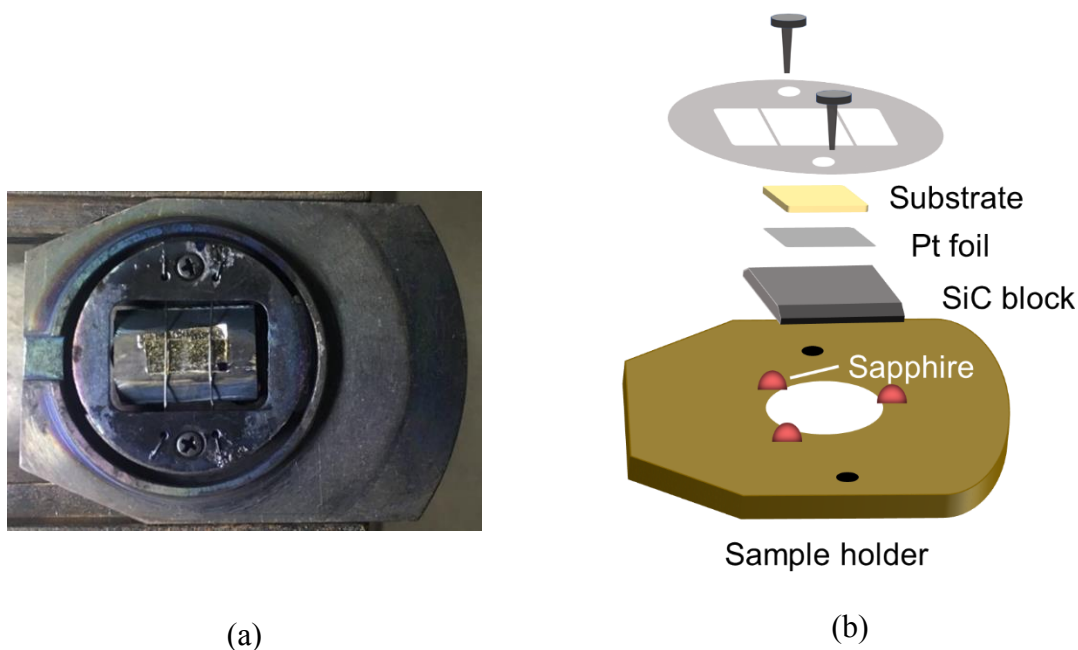


Fig. 3.3 (a) A photograph of a TiO₂ substrate mounted on the sample holder. (b) The sample holder construction.

3.3 Reflection high-energy electron diffraction

Reflection high-energy electron diffraction (RHEED) is used to investigate the surface morphology of films. In RHEED measurement, the sample surface is irradiated with an electron beam. In these experiments, the acceleration voltage was 25 to 30 kV and the incident angle was between 1 and 2 degrees. The diffracted electron beams can be seen on a phosphor screen. Due to the very low incident angle, electron diffraction is very surface sensitive and thus RHEED probes mostly the surface atomic layer structure.

Another advantage of the grazing incidence geometry is that RHEED measurement can be done during the deposition of films, so it is possible to observe the growth dynamics of thin films.

However, RHEED measurements are limited by the maximum oxygen pressure. In this study, the RHEED electron gun had only a single differential pumping stage, which limits the operation to an oxygen pressure of less than 10^{-3} Torr. When films were grown at higher pressures, RHEED measurements were done before and after the deposition of the film to record the surface morphology information.

On the RHEED screen, the diffracted beam positions mark the intersections of reciprocal lattice rods and the Ewald sphere, which define the surface diffraction

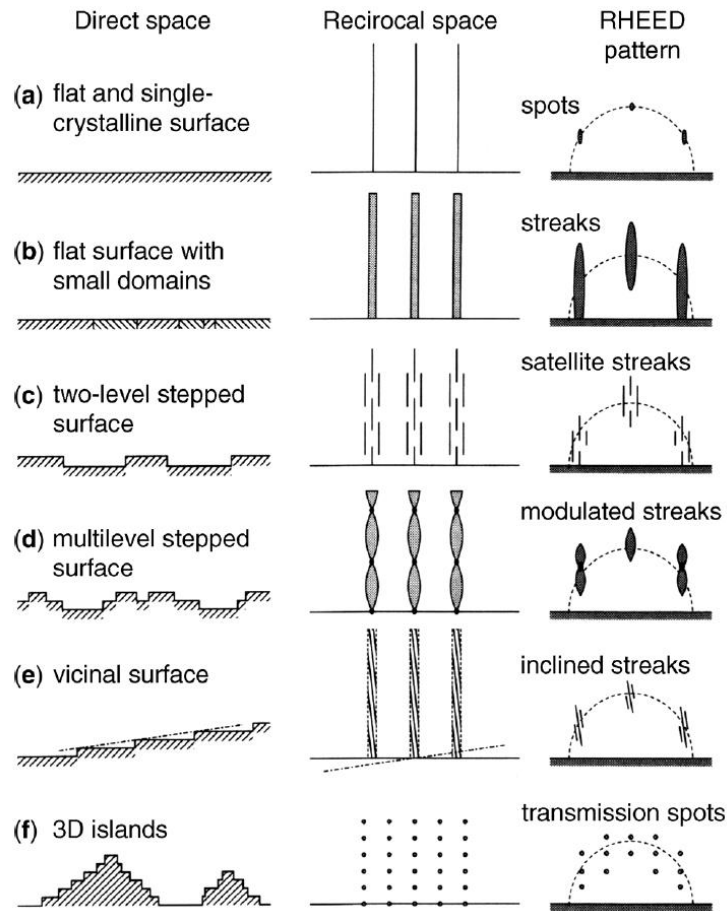


Fig. 3.5 Schematics of typical RHEED pattern observed in different surface

Atomic Force Microscopy

Atomic force microscopy is a scanning probe technique where the surface morphology is characterized on an atomic scale by scanning a sharp needle over the surface. In this work, a Shimadzu SPM-9600 microscope was used (Fig.3.6). One of the merits of AFM for oxide film characterization is that it does not require special surface treatment or ultra-high vacuum and surface morphology of insulating surfaces can be measured easily. Fig. 3.7 illustrates the operation principle of the AFM.

The microscope maintains a constant force between the tip and the surface. If the tip of the cantilever gets too close to the sample surface, the cantilever bends upward due to the contact force. When the tip is pulled away from the surface, an attractive force tends to bend the cantilever downward. If the elastic constant of the cantilever is known, the force between the tip and sample surface can be obtained quantitatively by measuring the cantilever displacement. By rastering the tip two-dimensionally over the



Fig. 3.6 A photograph of the Shimadzu SPM-9600 microscope on a vibration isolation table.

measurement area and measuring the force, a three-dimensional surface image can be obtained. In the Shimadzu microscope, the cantilever is stationary and the sample base is moved in x , y , and z directions by a piezo drive while a laser and a photodiode are used to monitor the movement of the cantilever (fig. 3.7). The incident laser light is reflected from the back of the cantilever and the position of the reflected light beam is detected with a segmented photodiode. The bending of the cantilever can be obtained by measuring the light intensity differences between the four segments of the photodiode detector. A vertical shift of the light spot corresponds to a change in the contact force. When the cantilever is far away from the sample surface, the optics is adjusted so that the light intensity entering the upper and lower parts of the photodiode is equal. Most of the AFM images in this work were taken in contact mode. In this case, when the AFM tip approaches the sample surface, the cantilever is pushed upwards and the computer adjusts the sample height until light intensity balance between the photodiode segments is restored. When the tip moves away from the sample surface, the cantilever bends downward and again, the computer readjusts the sample height to restore the light beam

to the original center position. The piezo stage height is then used to plot the height information as a function of the x, y coordinates. It is thus necessary to select appropriate scan speeds and feedback parameters so that the stage height information accurately represents the local height on the sample surface. Since the photodiode has four segments, it is possible to measure sideways tilting of the cantilever in addition to the up-down movement. This allows lateral friction forces imaging at the same time with topography measurement.

The scan area was usually $1\mu\text{m} \times 1\mu\text{m}$ or $5\mu\text{m} \times 5\mu\text{m}$. The spatial resolution is about 10 nm and the height resolution is on the order of 1 Å. To reduce noise in the measurements, the microscope was placed on a vibration isolation system (TS-150, Table Stable Ltd.).

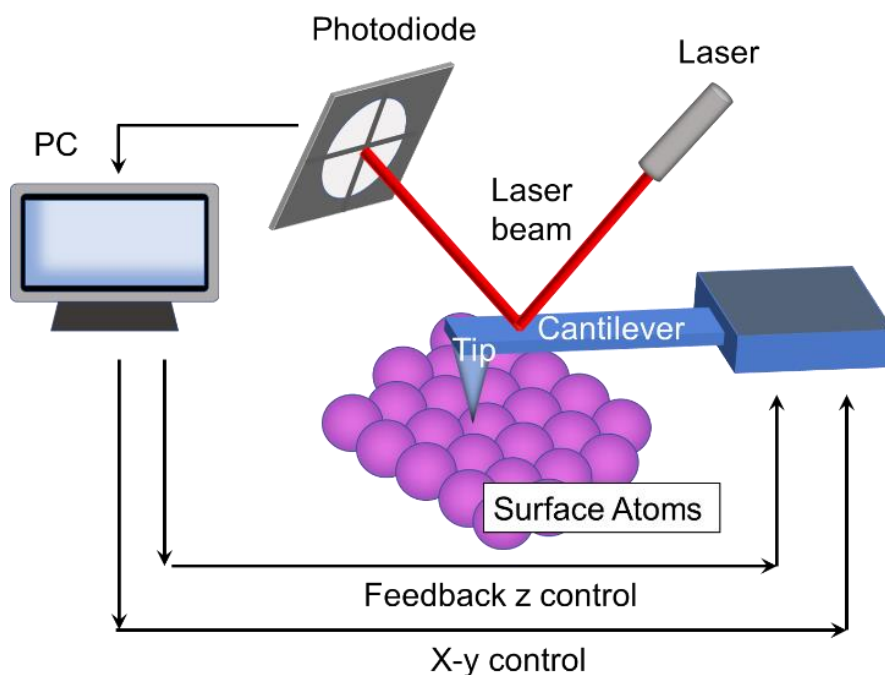


Fig. 3.7 Schematics of the operation of an atomic force microscope (AFM).

3.4 X-ray diffraction

X-ray diffraction (XRD) is a method for analyzing the structure of crystals. For thin films, XRD can be used to determine the film orientation, crystallinity, and the lattice parameters of the film samples.

When a thin film is irradiated with X-rays that have a wavelength that is close to the lattice spacing, diffracted X-rays interfere with each other. Only X-rays reflected at

specific angles that fulfill the Bragg's Law interfere constructively. Because the diffraction angle is dependent on the lattice parameter, the lattice parameter of the film can be determined by measuring the diffraction angle.

Fig.3.8 shows the schematic of x-ray diffraction at the surface of a crystal, where d_{hkl} is the lattice spacing and θ is incident angle. The path length difference for two x-rays reflected from the first plane and second planes is $2d_{hkl} \sin\theta$. Constructive interference occurs between these two reflected x-rays only when the path difference is an integer multiple of the wavelength λ . This diffraction condition is shown in the Eq. 3.1, where n is a positive integer.

$$2d_{hkl} \sin\theta = n\lambda \quad (3.1)$$

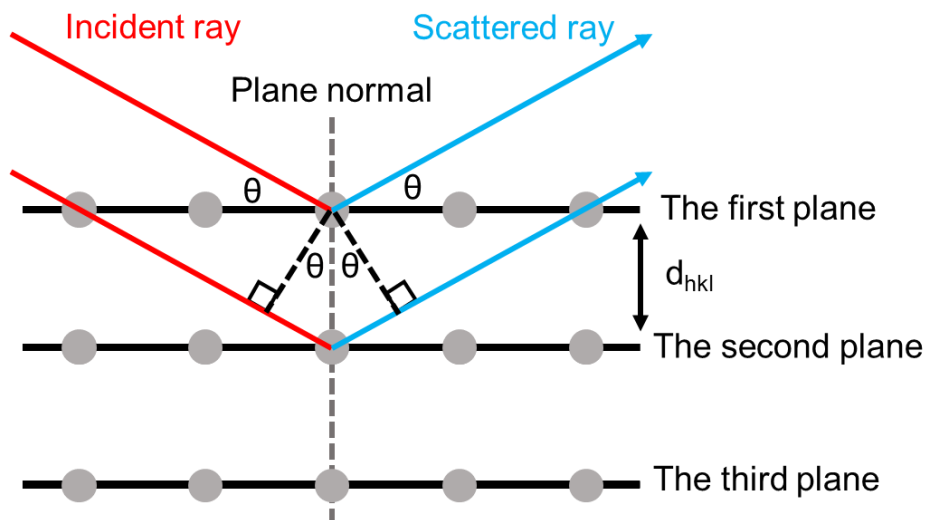


Fig. 3.8 Bragg's Law and diffraction at the crystal surface.

In this study, $\omega - 2\theta$ scans were used to measure the out-of-plane lattice parameter of the films with a X'Pert MRD diffractometer from Philips. Fig. 3.9 shows the measurement geometry of this 4-axis XRD instrument. The ω angle defines the orientation of the sample relative to the x-ray source (the incident angle), and the 2θ angle defines the position of the detector. In $\omega - 2\theta$ scans, the diffractometer scans the detector 2θ angle while maintaining the symmetric diffraction condition where ω is equal to θ . Independent θ and ω scans are used for sample surface alignment and for measuring rocking curves for characterizing the crystallinity of a film.

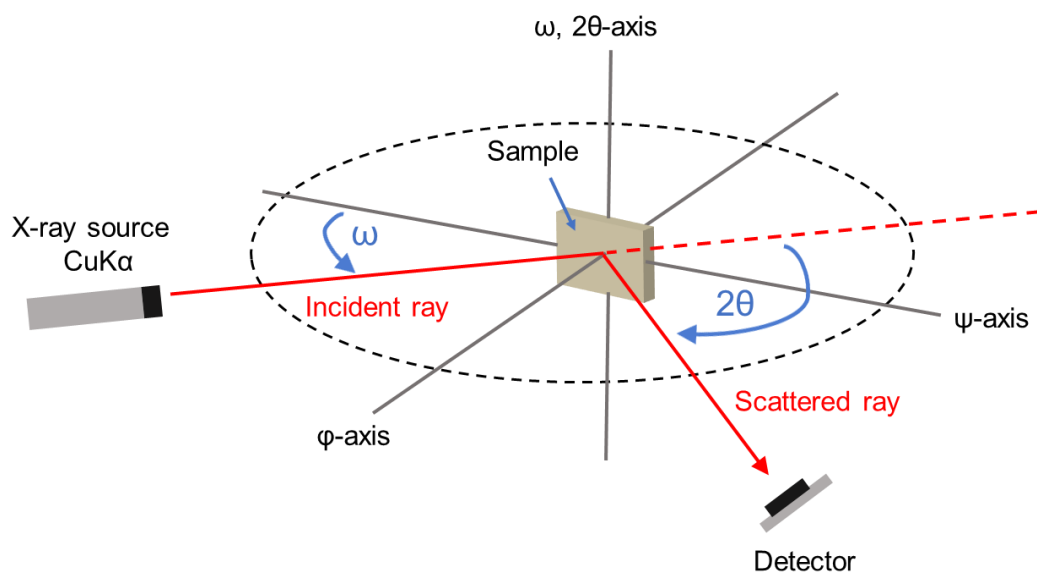


Fig. 3.9 Schematics of the geometry of the 4-axis XRD. The 4-axis, ω , 2θ , ϕ , and ψ are shown.

4 Freestanding film of BaTiO₃

4.1 Introduction

The key building block of ferroelectric vibration energy harvesting devices is a flexible ferroelectric thin film that is attached to two electrodes. One possible ferroelectric material is BaTiO₃ and it was selected for this project due to the relatively high polarization values that can be achieved in BaTiO₃ thin films. However, high-quality BaTiO₃ films with a well-defined out-of-plane polarization direction can only be grown on crystalline substrates that cannot be flexed. The purpose here is thus to develop a process for fabricating freestanding BaTiO₃ film that are separated from a crystalline substrate after film growth. Usually, functional oxides need to be deposited at high temperatures to obtain epitaxial films with high crystallinity and physical properties that match bulk behavior. For oxide thin films, the usual growth temperatures range from 600 °C to over 1000 °C. However, flexible substrates like polymers have low decomposition temperatures and crystalline functional oxides cannot usually be deposited directly on flexible substrates. One possible approach to this problem is to

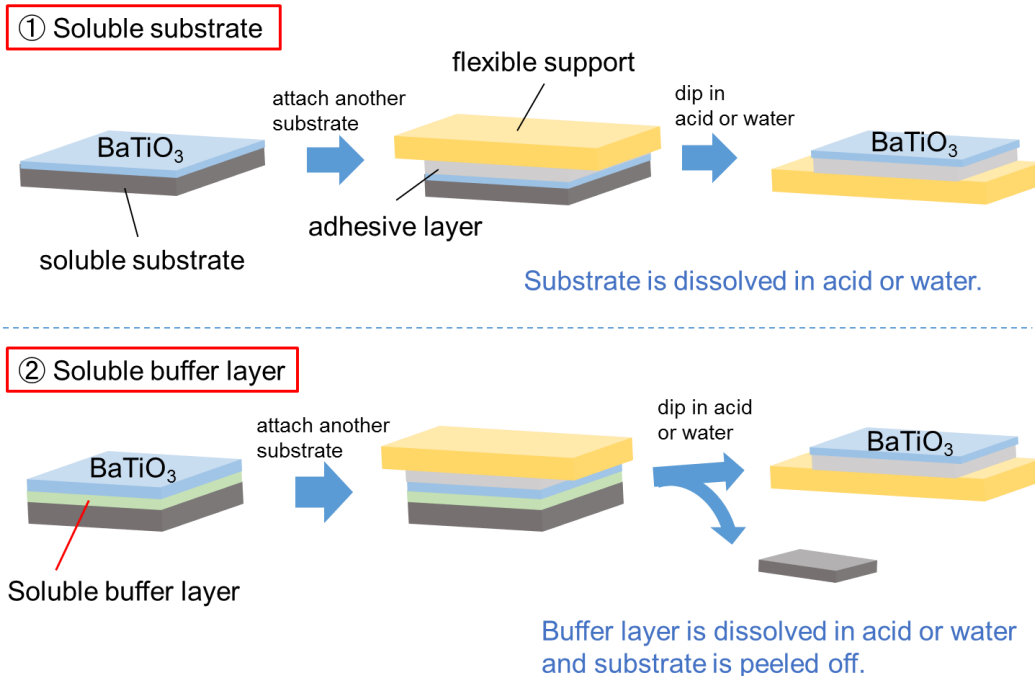


Fig. 4.1 Two possible methods of transferring a BaTiO₃ thin film from a single crystal substrate to a flexible support: ① dissolving the substrate, ② using a soluble buffer layer.

grow a thin film on a rigid single crystal substrate and then transfer the film to a flexible support.

Fig 4.1 shows two examples of the transfer process, both of which were attempted. The first method involves the etching of the substrate itself. This is a possible option for substrate materials that can be etched in water (halide substrates) or in an acid that doesn't damage the BaTiO₃ film. At first, a BaTiO₃ film is deposited on the single crystal substrate. The film is then attached to a flexible support, such as a polymer sheet by using an adhesive layer. Finally, the film is placed in water or acid and the substrate is allowed to dissolve slowly. Assuming that the acid doesn't damage the BaTiO₃ film, the bare film is now supported on a flexible plastic sheet.

The second method requires the use of a buffer layer that is soluble in water or acid. At first, the buffer layer is deposited on the single crystal substrate, followed by the growth of a BaTiO₃ film. After deposition, the top side of the sample is attached to a flexible support sheet using an adhesive layer. When this sample is dipped in acid or water, only the buffer layer is dissolved and the original single crystal substrate is detached from the film. The BaTiO₃ film can thus be transferred to a plastic support and the original substrate can be recovered.

4.2 Using a Ge substrate

4.2.1 Growing a BaTiO₃ film on a Ge substrate

Germanium can be used as a soluble substrate material that is relatively well lattice matched with BaTiO₃. The advantage of using a soluble substrate is that the sample structure is simple; a film is grown on a substrate, which is then removed. Using a soluble buffer layer would require the growth of two different materials, which may degrade the crystal quality of the BaTiO₃ layer.

Germanium was selected as a soluble substrate for BaTiO₃ film growth because germanium can be dissolved in an aqueous H₂O₂ solution [27] and the lattice mismatch between BaTiO₃ and Ge is very small (0.92%). However, Ge substrates require preparation before film growth.

Before deposition of BaTiO₃, the Ge substrates were etched in a buffered HF solution and annealed in the vacuum chamber to desorb the native oxide and form a well-defined (2×1) surface reconstruction of the Ge (001) surface.

Fig. 4.2 (a) shows a RHEED image of a Ge (001) substrate that was etched in 5% HF

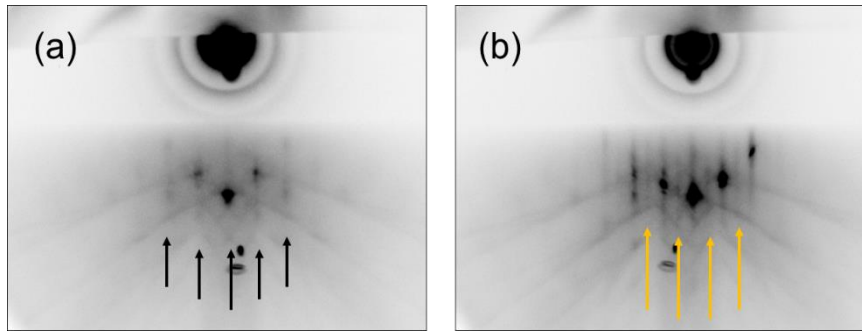


Fig. 4.2 RHEED images of a Ge substrate surface (a) before and (b) after annealing at 550 °C. Black arrows indicate (1×1) diffraction pattern and yellow arrows indicate half order diffraction streaks of (2×1) reconstruction surface.

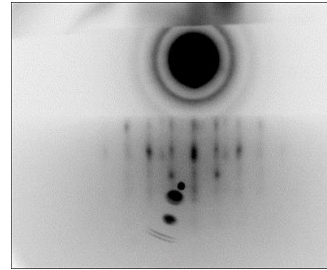
aqueous solution for 20 min and (b) annealed for 10 min at 550 °C under UHV conditions. The (2×1) surface reconstruction that forms after the native oxide is removed by a deoxidizing UHV anneal at 550 °C can be seen in Fig. 4.2 (b). [28]

The BaTiO₃ films were fabricated on Ge substrates after the surface treatment. The film thickness was 500 nm. For deposition, the ablation laser pulse rate was 5Hz, giving a growth rate of ~0.0095 nm/pulse. The deposition temperature was 600 °C and the deposition was done at the chamber base pressure of 10⁻⁷ Torr. The properties of this sample are summarized in Fig. 4.3.

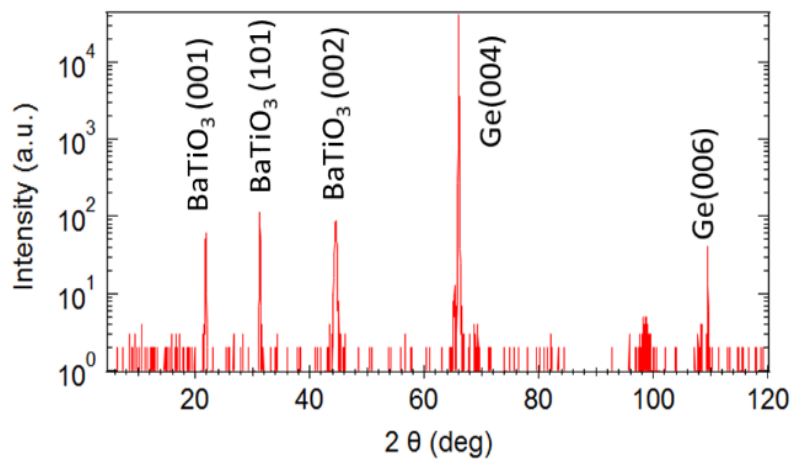
The presence of BaTiO₃ (001) and (101) diffraction peaks in the XRD pattern showed that the film contained a mixture of several crystal orientations despite the good lattice matching of BaTiO₃ with the Ge substrate. One possible process parameter that can affect the microstructure of the film is the oxygen pressure. On oxide substrates, a growth pressure of 10⁻⁶ Torr or higher is common for BaTiO₃ films. For optimizing the oxygen pressure, another sample was therefore made at an oxygen background pressure of 2×10⁻⁵ Torr while keeping other deposition parameters the same as before. As shown in Fig. 4.4, the Ge substrate became white after the deposition of BaTiO₃. It is clear that feeding oxygen into the growth chamber during BaTiO₃ deposition leads to re-oxidation of the Ge substrate surface at the 600 °C film growth temperature. It is thus clear that an oxygen environment cannot be used and it would be difficult to obtain high-quality BaTiO₃ films on Ge.



(a)



(b)



(c)

Fig. 4.3 (a) Surface image of BaTiO₃ film on a Ge substrate. (b) RHEED image of the BaTiO₃ film after deposition. (c) XRD pattern of the BaTiO₃ film sample.



Fig. 4.4 sample picture of a BaTiO₃ film grown on a Ge substrate at an oxygen background pressure of 2×10^{-5} Torr at 600 °C.

4.2.2 Etching process of a Ge substrate

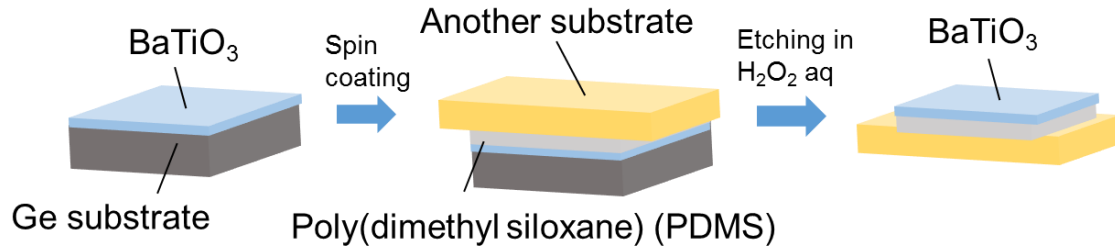
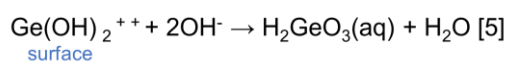
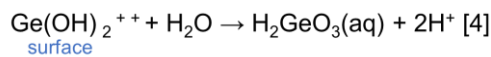
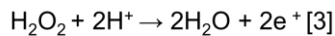
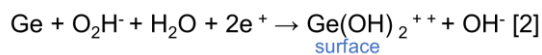
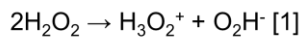


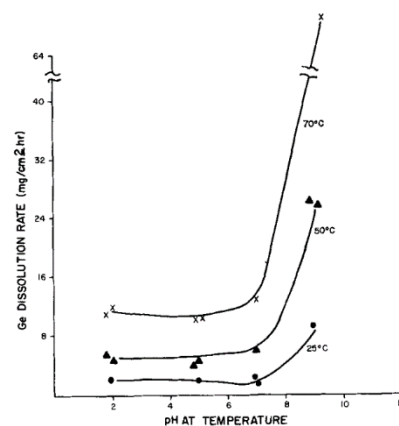
Fig 4.5 Details of the film transfer process by etching the Ge substrate.

As the first step of the transfer process, the transfer substrate was covered with an adhesive layer of poly(dimethyl siloxane) (PDMS) by spin coating and the BaTiO₃ film sample was pressed onto the adhesive layer. After that, the Ge substrate was dissolved in H₂O₂ aq (Fig 4.5). The Ge etching reaction is quite slow and the substrate volume is large, which is why it was necessary to optimize the etching conditions for achieving the optimal etching rate.

The reaction steps of dissolving Ge in H₂O₂ are shown in fig. 4.6(a) [27]. The formation of the final dissolution products, metagermanic acid (H₂GeO₃(aq)), can proceed by one of two reactions, Eq. [4] and [5]. In solution of low pH, the final dissolution reaction is considered to proceed primarily according to Eq. [4], but with increasing pH, the reaction with OH ions becomes more important and reaction [5] predominates. As shown in fig. 4.6(b), the pH of H₂O₂ aq is also an important factor that



(a)



(b)

Fig 4.6 (a) The mechanism of etching Ge by H₂O₂. (b) Dependence of dissolution rate on pH in a 15% H₂O₂ aqueous solution [27].

affects the dissolution rate. It is clear from the plot that the dissolution rate increases with pH. The pH of the etchant was adjusted by mixing 5% KOH aq and deionized water in 30% H₂O₂ aq.

Fig. 4.7(a) shows the dissolution rates for several compositions of the etching solution. From this result, the best composition was 25mg 5% KOH : 5mg 30% H₂O₂ aq : 25mg deionized water. Fig 4.7(b) shows the effect of reaction temperature on the Ge etching. Temperature has a significant effect on the dissolution rate above 100 °C and higher temperatures can be used to dissolve the whole Ge substrate in few hours.

The thin film transfer process was tested by attaching a BaTiO₃ sample to a Si substrate (fig.4.8(a)). A Si substrate was covered with a thin PDMS layer by spin coating and the BaTiO₃ film was pressed face down onto the PDMS adhesion layer. The sample was heated at 105 °C for 15 min. The Ge substrate was then dissolved in the optimal etching solution at 100 °C (fig. 4.8(b)). As an be seen in the photograph, the Ge substrate was completely dissolved, exposing the Ge film on the PDMS adhesion layer. Unfortunately, no BaTiO₃ diffraction peaks could be observed by XRD, which indicates that the BaTiO₃ was also damaged by the etching procedure.

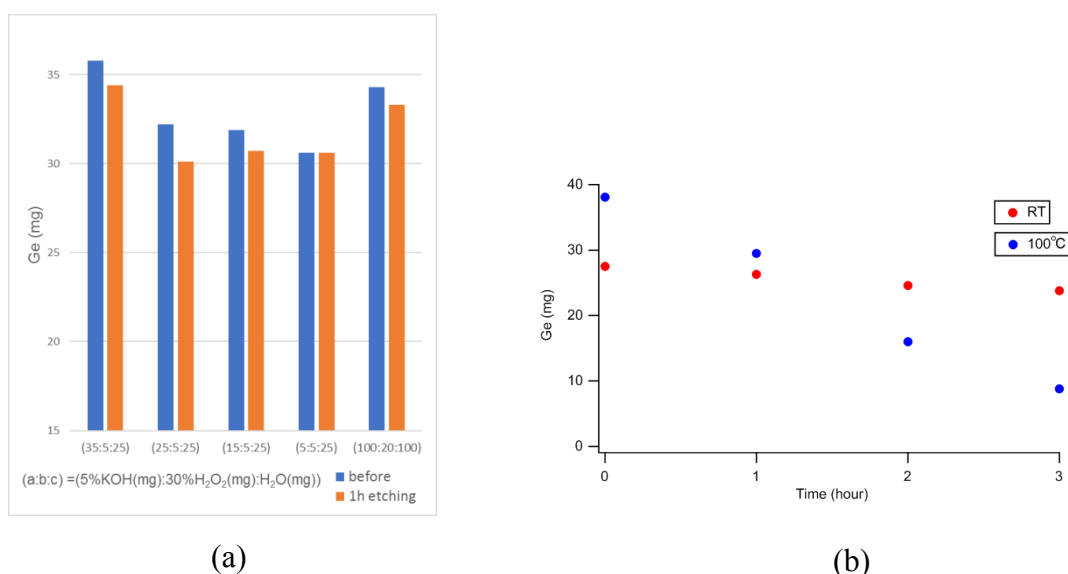


Fig 4.7 (a) Weight loss of a Ge substrate for several etchants consisting of KOH and H₂O₂ aq. (b) Difference of Ge substrate weight loss at different temperatures in a solution of 5%KOH(mg) : 30%H₂O₂(mg) :H₂O (mg) = 25: 5 : 25.

BaTiO₃ film under Ge substrate

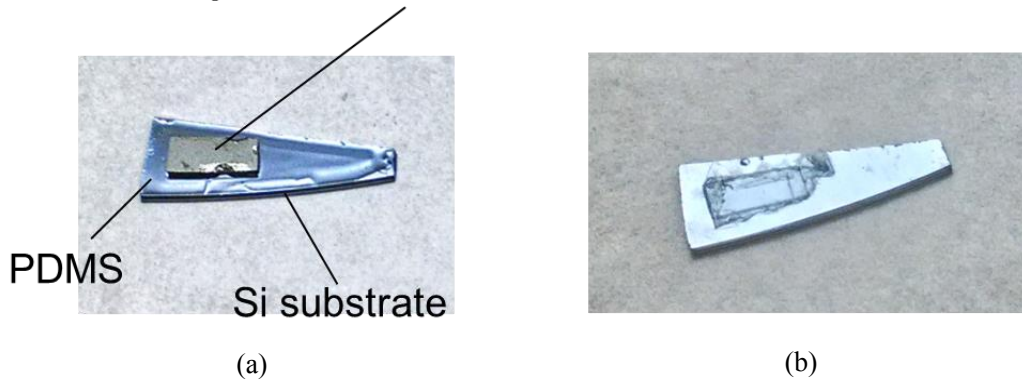


Fig 4.8 The actual sample which was attached to Si substrate for practice by PDMS before (a) and after (b) etching the Ge substrate.

Additional experiments were therefore done to check the chemical stability of BaTiO₃ films in the etching solution. An epitaxial BaTiO₃ film grown on a SrTiO₃ substrate was dipped in the same etching solution at 100 °C for 4 hours. XRD patterns were measured before and after the dip in the etchant. Fig. 4.9 shows the result of the XRD measurements. The intensity of the BaTiO₃ peak dropped and the diffraction peak shape changed, indicating that the BaTiO₃ film was damaged by the H₂O₂ solution.

Based on the XRD analysis, it was concluded that it is unlikely that all of the film was dissolved in the Ge substrate etching experiment. However, it was clear that this transfer process using the H₂O₂ etching solution for removing a Ge substrate is not suitable for obtaining high-quality freestanding BaTiO₃ films.

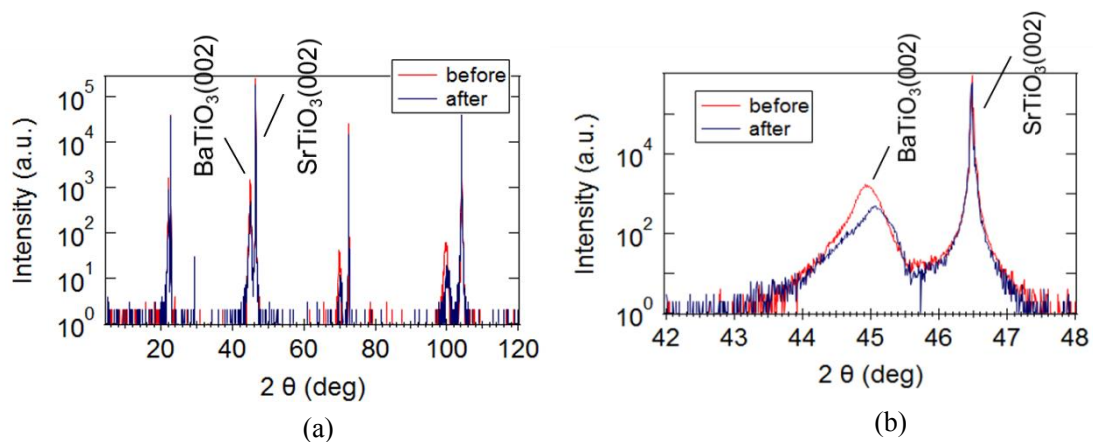


Fig 4.9 The overlapped XRD patterns of an epitaxial BaTiO₃ film on SrTiO₃ before and after etching in H₂O₂.

4.3 Using a water-soluble layer

4.3.1 Fe₃O₄/BaO/SrTiO₃

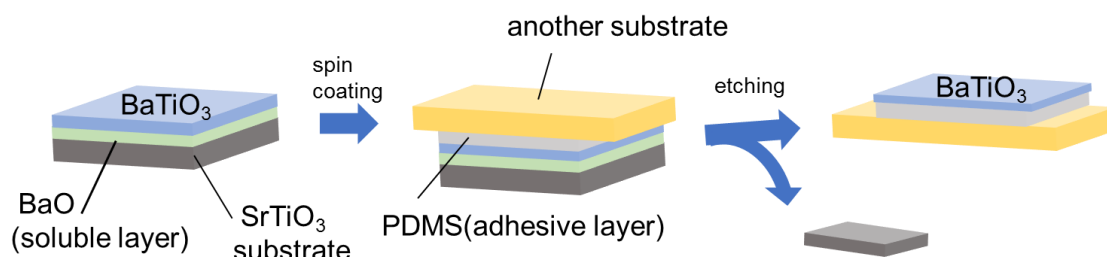


Fig 4.10 Details of the transfer process using a water-soluble BaO buffer layer.

Another attempt was made to fabricate a freestanding film by using a water-soluble buffer layer (fig. 4.10). In this process, a BaO buffer layer is deposited before the deposition of the BaTiO₃ film. BaO was selected among some sacrificial layer because its lattice parameter is close to SrTiO₃ and BaTiO₃. The lattice mismatch along c-axis is 0.20 % between BaO and SrTiO₃, and 2.1 % between BaO and BaTiO₃, so BaO and BaTiO₃ films are considered to grow epitaxially on SrTiO₃ substrate. BaO reacts rapidly with H₂O and dissolves in just a few seconds as shown in fig. 4.11. Here, a thick BaO layer was grown on a Si substrate through a stencil mask for film thickness measurement with the Dektak profilometer. This thickness calibration sample was dipped in water for 10 s, after which the film had dissolved.

The film transfer process is similar to the Ge etching case. As the former process, another support sheet is coated with PDMS by spin coating and the film sample is attached face down to the adhesion layer. The sample is then dipped in deionized water, which only dissolves the highly reactive BaO layer.

Since the BaTiO₃ films used in this study for flexible devices are very thin, about a few hundred nanometers, the films are nearly transparent and it can be hard to see that the

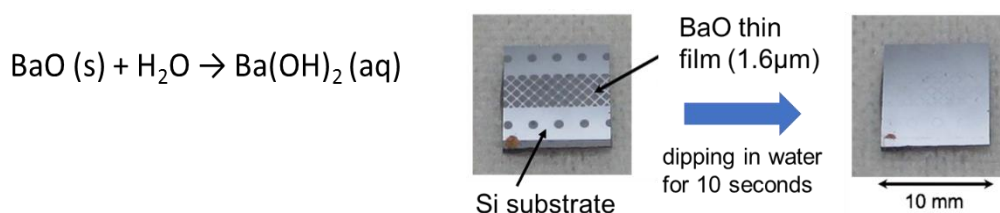


Fig 4.11 Reactivity of BaO with water.

thin film is actually transferred to another substrate. Before preparing BaTiO₃/BaO/SrTiO₃(substrate), Fe₃O₄/BaO/SrTiO₃ test samples were prepared for optimizing the transfer process. Magnetite Fe₃O₄ film were used because Fe₃O₄ is black in color and thus easy to see during sample processing.

Fig. 4.12 shows pictures of a Fe₃O₄/ BaO/SrTiO₃ sample where the film thickness was about 170 nm as measured by profilometry. The BaO layer thickness was estimated to be about 120 nm from the RHEED oscillation period. For deposition, the laser pulse rate was 1 Hz for the BaO and 10 Hz for the Fe₃O₄ layer growth, giving deposition rates of 0.033 nm/pulse and 0.0028 nm/pulse, respectively. The deposition temperature was 400 °C and the ambient oxygen pressure was 2×10^{-6} Torr for both BaO and Fe₃O₄ growth.

As we can see in fig. 4.12, the film surface appears rough already when the film was exposed to air. The film was peeled off the substrate in some places after water dipping. It thus appeared likely that the BaO buffer layer reacted with humidity in air and transformed the film surface, causing the film to fracture and delaminate in water. Since the formation of hydroxide leads to layer expansion, using a thick BaO layer would cause large mechanical stresses in the films in humid air or in water. The Fe₃O₄ layer should thus be thicker than the soluble buffer to make it more rigid. To solve this problem, another sample (Fe₃O₄/ BaO/SrTiO₃) was made with a thinner BaO layer (40 nm) and a thicker Fe₃O₄ layer (760 nm).

Fig. 4.13 shows a picture of this sample and XRD analysis results. The total film thickness was about 800 nm. The deposition conditions were the same as the former sample. In this sample, the surface did not appear damaged after exposure to air and there is a sharp Fe₃O₄ peak in the XRD pattern. The transfer process was tested using this sample.

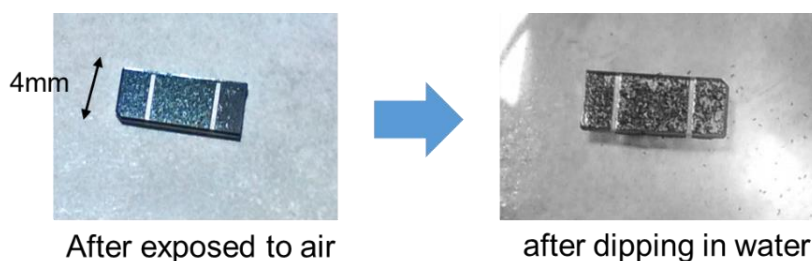
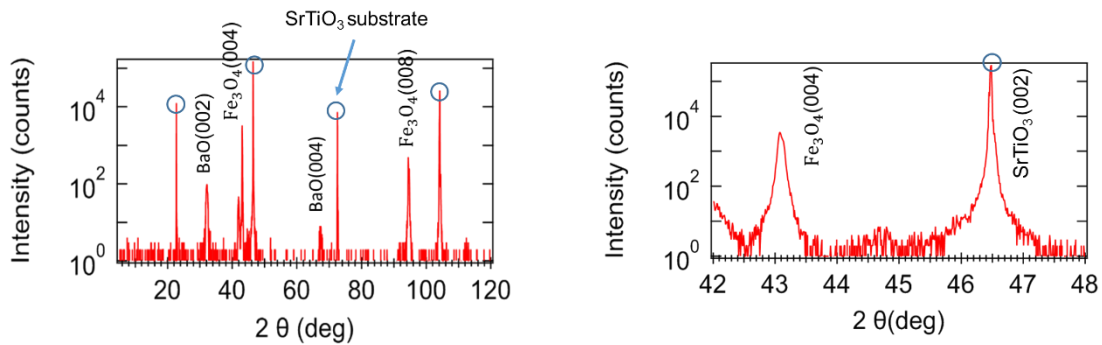


Fig 4.12 Photographs of a Fe₃O₄/ BaO/SrTiO₃ test sample before and after dipping in water.



(a)



(b)

Fig 4.13 (a) Surface picture and (b) XRD wide and narrow scans of a 800 nm thick Fe₃O₄/ BaO/SrTiO₃ sample.

4.3.2 Etching process of BaO

Water can reach the BaO buffer layer either from the edges of the film or through the film if the BaTiO₃ or Fe₃O₄ layer is thin and permeable to water, for example, due to grain boundaries or other defects. To allow more efficient access to water from the sides of the sample, the edges of the film, which may have been coated by Fe₃O₄ during film growth, were cut off. The thin film sample was then attached to a microscope slide cover glass with a PDMS adhesive layer that was spin coated on the glass before attaching the film sample. The sandwich structure was heated at 100 °C for 30 min and then left soaking in water for two days. The original SrTiO₃ substrate was completely removed from the glass substrate and the 800 nm Fe₃O₄ film remained on the glass substrate. The first successful film transfer is shown in fig 4.14. Fig. 4.15(a) shows the XRD patterns of a freestanding Fe₃O₄ film that was transferred onto a glass substrate. Since the substrate was removed, no substrate peaks can be seen in fig. 4.15(a). A comparison of the original XRD pattern taken before transfer with a pattern taken after the transfer is shown in fig. 4.15 (b). The XRD data thus shows that only the Fe₃O₄ film

part of the original $\text{Fe}_3\text{O}_4/\text{BaO}/\text{SrTiO}_3$ structure was transferred to the glass plate and the Fe_3O_4 film crystallinity did not change during this process.

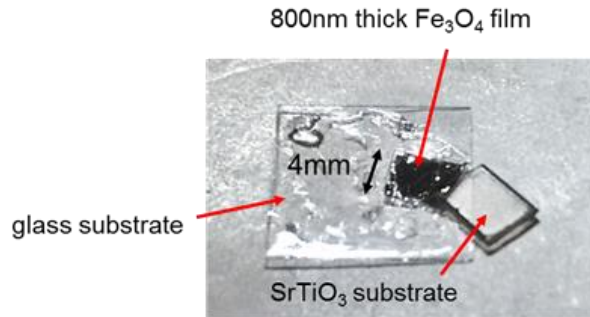


Fig 4.14: Freestanding Fe_3O_4 film transferred to glass substrate.

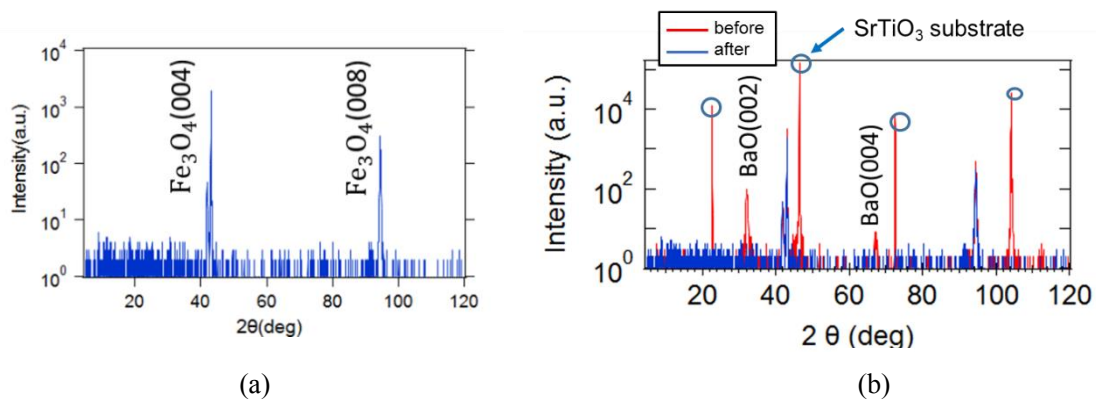


Fig 4.15 XRD peaks of a Fe_3O_4 film after transfer to a glass sheet (a), Comparison of XRD patterns taken before (red) and after (blue) film transfer (b)..

4.3.3 BaTiO_3 film on a BaO buffer layer

After successful transfer of a Fe_3O_4 film from a SrTiO_3 substrate to a glass carrier, a similar $\text{BaTiO}_3/\text{BaO}/\text{SrTiO}_3$ multilayer structure was prepared for transfer. Unlike the magnetite case that was illustrated in figs. 4.14 and 4.15, the transfer process for BaTiO_3 was more strongly affected by atmospheric humidity. A camera image of the BaTiO_3 film before transfer processing, taken immediately after unloading from the deposition chamber, is shown in Fig.4.16. Film thickness was about 300 nm and the BaO layer thickness was about 80 nm. For deposition, the laser pulse rate was 1 Hz (BaO layer) or 5 Hz (BaTiO_3 layer). The growth rates were 0.033 nm/pulse for BaO and 0.012 nm/pulse for BaTiO_3 . The BaO deposition temperature was 400 °C, while 600 °C was

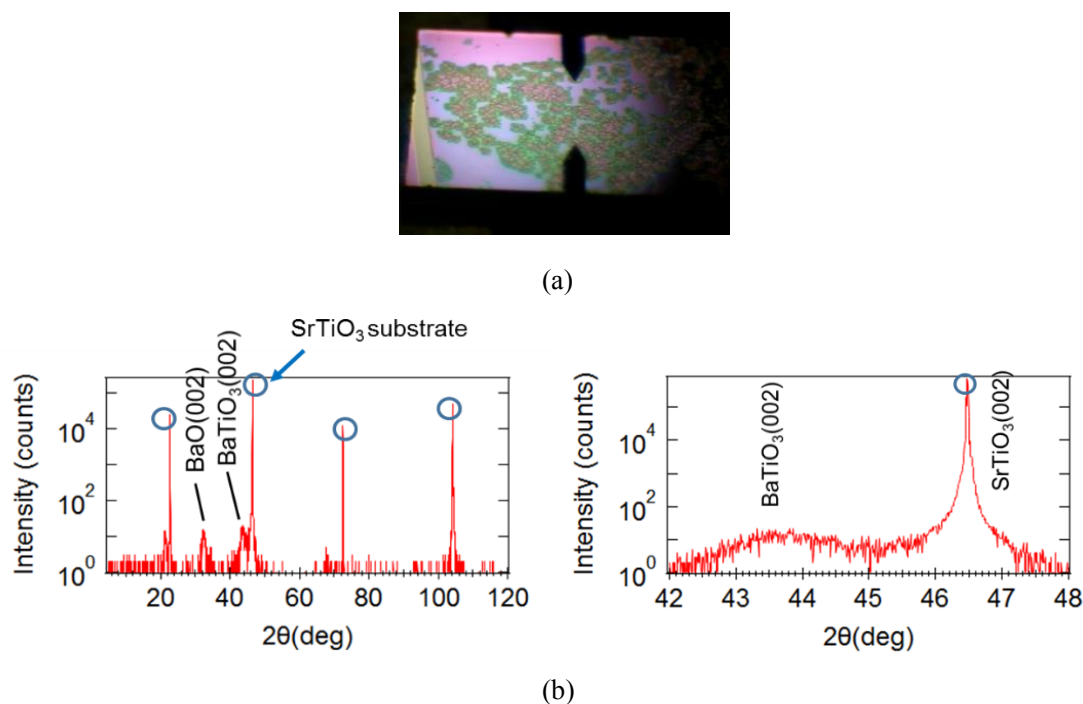


Fig 4.16 (a) Surface picture and (b) XRD peaks of a 300 nm thick BaTiO₃/ BaO/SrTiO₃ sample.

used for BaTiO₃ growth to obtain better crystallinity. The oxygen pressure was 2×10^{-6} Torr for both layers.

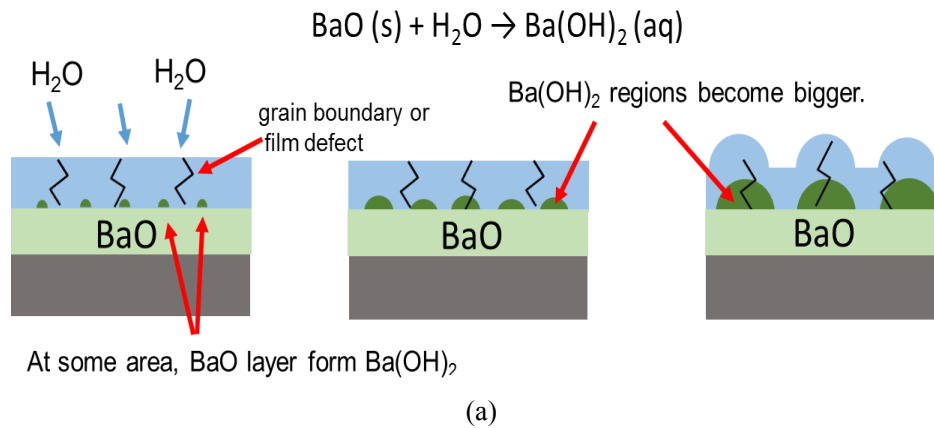
There were two problems with this sample. One is that BaTiO₃ didn't grow epitaxially on the BaO layer. The intensity of the BaTiO₃(002) peak is very small and broad as shown fig. 4.16 (b). It thus appears that BaO is not a good template for BaTiO₃ to grow. One possible way to solve this problem is to insert a buffer layer between the BaTiO₃ layer and the BaO layer. Lattice mismatch between the film and the substrate is one of the main factors for determining the crystallinity of a thin film. In this respect, SrTiO₃ is a good buffer layer because the lattice mismatch between SrTiO₃ and BaO is much lower (0.20%) than the lattice mismatch between BaTiO₃ and BaO (2.1%). Thus, a thin SrTiO₃ template layer was inserted between BaO and BaTiO₃ in later samples.

The other problem is the roughness of the film surface. As shown by the camera image in fig. 4.16 (a), many defect spots appear randomly over the film surface upon air exposure. The observed roughness increased in time on the scale of minutes, which suggests that the roughening is related to atmospheric moisture.

My hypothesis is that water can permeate the BaTiO₃ layer through grain boundaries, which appear to be abundant, based on the low crystallinity of the film, and thus react with BaO over a time scale of minutes. Fig. 4.17 shows a schematic view of this mechanism.

From preliminary experiment, it is known that the atmospheric moisture penetration can be prevented by a magnetite film. For this reason, a Fe_3O_4 capping layer was added to later samples, which had the following layer order: $\text{Fe}_3\text{O}_4(\text{cap})/\text{BaTiO}_3/\text{SrTiO}_3/\text{BaO}/\text{SrTiO}_3(\text{substrate})$. Deposition conditions and the sample properties are shown in fig. 4.18. The total film thickness was about 650 nm and the thickness of the BaO layer and the SrTiO_3 buffer layer were about 150 nm and 30 nm, respectively. Although some small bumps formed on the surface of the sample in air, the surface condition was considerably improved compared to the original $\text{BaTiO}_3/\text{BaO}/\text{SrTiO}_3$ sample.

This sample was attached to a microscope slide cover glass with PDMS as was explained in Chapter 4.3.2. The original SrTiO_3 substrate was removed completely after soaking the sample in water for one day (fig. 4.19). Even though the film was still damaged the lift-off process, the BaTiO_3 film could be transferred successfully from a SrTiO_3 substrate to a glass plate.



	BaO	Ba(OH)_2
Crystal structure	cubic	Monoclinic
Mass density (g/cm^3)	5.72	3.74
Mol mass (g/mol)	153.3	171.3
Mol volume (cm^3/mol)	26.8	45.8

(b)

Fig 4.17 (a) Assumed mechanism of surface damage of the sample. H_2O may permeate the BaTiO_3 film through grain boundaries or other defects and react with the BaO layer, forming a hydroxide. Since the hydroxide formation expands the BaO layer thickness locally around the penetration point, local roughness would increase. (b) Calculated Mol volume of BaO and Ba(OH)_2 . Ba(OH)_2 is much larger than BaO which contains same amount of Ba ions.

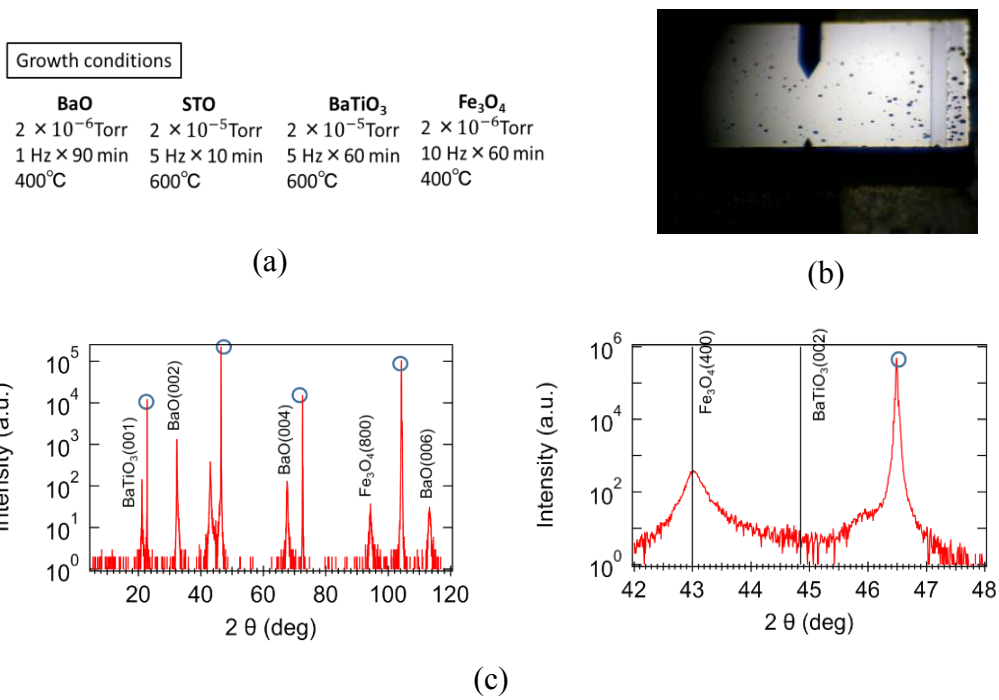


Fig 4.18 Growth conditions and film properties of the sample (Fe₃O₄/BaTiO₃/SrTiO₃/BaO/SrTiO₃).

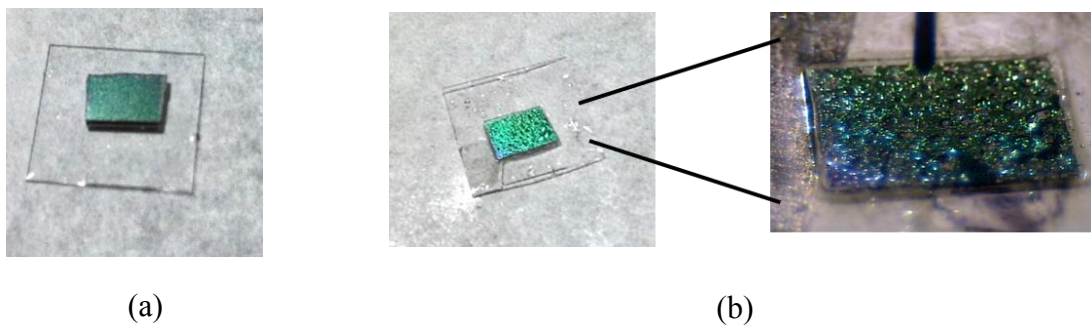


Fig 4.19 (a) The actual sample (Fe₃O₄/BaTiO₃/SrTiO₃/BaO/SrTiO₃) attached to a cover glass. (b) The transferred BaTiO₃ film on the glass substrate.

5 Sensing local strain in thin films

5.1 Introduction

Strain in flexible membrane devices, such as vibrational energy harvesters, is generally not uniform. It is possible to analyze the strain state by measuring the deflection profile of a membrane and use an elastic model to estimate the local in-plane strain distribution, but this analysis assumes that the elastic parameters of all layers in a device structure are known. Another possible solution is to use a strain sensing layer as a part of the energy conversion device design.

In this Chapter, I discuss the measurement of local strain by using a VO₂ thin film as a built-in strain sensor. The Chapter is divided into 3 main sections, starting with a discussion of the thin film fabrication and characteristics. The second section is about the construction of a crystal bending stage and the measurement system. The third section is about the optical properties of a VO₂ thin film during bending. The reflectance change of a VO₂ thin film was measured while it was deformed by the crystal bending stage.

5.2 Fabrication of VO₂ thin films on TiO₂ substrates

5.2.1 TiO₂ substrate

The benefit of a built-in strain sensor in a flexible device is that it accurately measures the local strain in the surface layer of a membrane device. The strain sensing film thus has to be thin enough to be fully strained on the underlying surface and not show additional strain relaxation under strain. Considering that typical misfit relaxation thickness in oxide thin films is around 10 nm, it is reasonable to consider VO₂ films of similar thickness.

Before the deposition of VO₂ thin films an attempt was made to obtain an atomically flat TiO₂(001) surface to obtain nanometer-scale films with good crystallinity and well-defined misfit strain state. To get a flat surface with a step-and-terrace morphology, TiO₂ substrates were annealed at various temperatures. A high-temperature electric

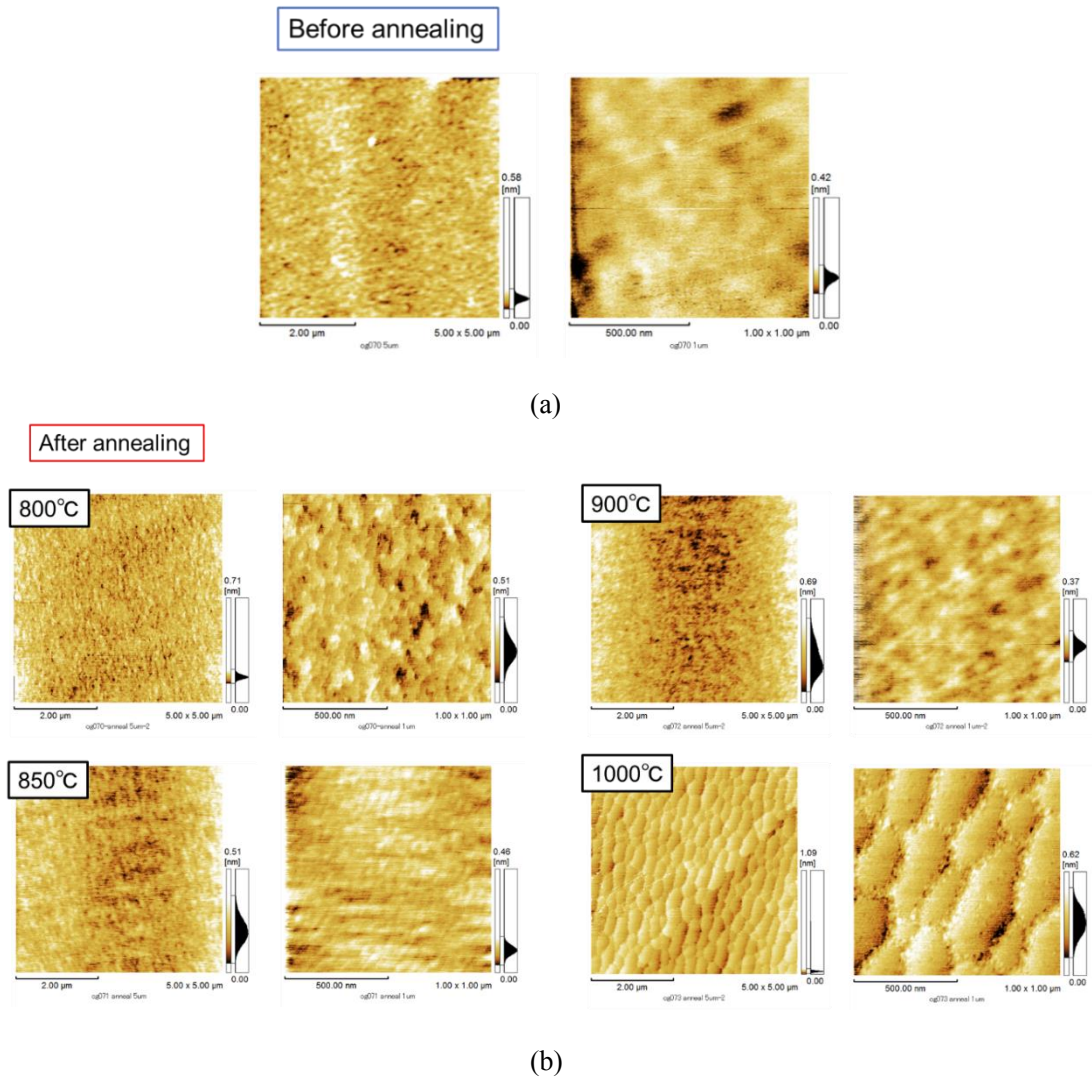


Fig. 5.1: AFM images of 0.5 mm thick $\text{TiO}_2(001)$ substrate (a) before annealing and (b) after annealing at various temperatures. Left image is area of $5 \times 5 \mu\text{m}^2$, right image area is $1 \times 1 \mu\text{m}^2$.

furnace (MSFT-1020) was used to anneal the substrates in air. Fig. 5.1 (a) shows wide-area and high-resolution AFM images of the surface of a 0.5 mm thick $\text{TiO}_2(001)$ substrate before annealing. The polished surface was flat on average, with height variations of less than a nanometer over the $5 \times 5 \mu\text{m}^2$ imaging area, but surface steps were not visible. Fig. 5.1 (b) show the surface of the same substrate after it was annealed in air for 3 h at 800 °C, 850 °C, 900 °C, and 1000 °C. The best temperature to obtain a flat surface with a clear step-and-terrace morphology was 850 °C. The surface diffusion appears to be too slow at 800 °C to form a uniform terrace structure, while a peculiar roughening structure was seen above 900 °C. An XRD scan of this substrate is shown in Fig. 5.2. Based on the annealing tests, all TiO_2 substrates were annealed in air at 850 °C before VO_2 thin film deposition.

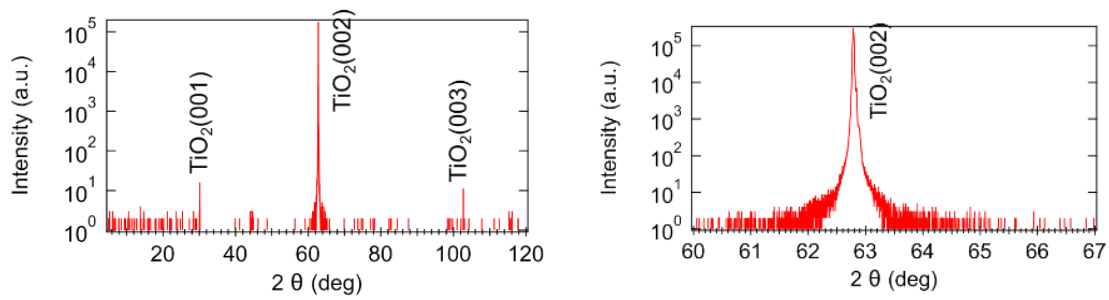


Fig. 5.2 : XRD pattern of a TiO_2 substrate, taken after annealing in air for 3 h at 850 °C. The left plot shows a wide scan with a narrow scan near the (002) peak shown on the right.

5.2.2 Structural and electrical properties of VO_2 films

Various physical properties of VO_2 thin films, such as the metal-insulator transition (MIT) temperature, the magnitude of the resistance change at the MIT, and the hysteresis width of the resistance change were measured for films grown under different deposition conditions. It is known that the VO_2 MIT temperature, transition sharpness, and hysteresis depend on the strain state of the film [23,29]. The best properties to optimize for in film growth thus depend on the particular purpose. For example, VO_2 microbolometers used in infrared thermography benefit from a broad transition although the temperature sensitivity is somewhat reduced. For the purpose optical reflectance change measurement in a VO_2 thin film strain sensor, the sharpest transition near room temperature is the most convenient, since energy harvesting devices generally work at ambient temperatures and the highest possible sensitivity to strain is required for imaging the strain distribution.

As a first step, it is necessary to stabilize the VO_2 phase in a thin film grown from a VO_x target. The oxygen background pressure was therefore optimized by maximizing the resistance change at the MIT. Fig. 5.3 shows the structural and transport properties of several VO_2 thin films grown on TiO_2 substrates at various oxygen pressures. The film thickness was 20 nm for all samples, the ablation laser fluence on the target surface 0.56 J/cm² and the pulse rate was 2 Hz. At a growth temperature of 440 °C, a growth rate of ~0.0040 nm/pulse was obtained. A 20 nm film thus required about 5000 laser shots and took about 1.5 hours to grow.

The XRD patterns show a sharp TiO_2 substrate (002) peak at a 2θ value of about 62.8° with a slight shoulder on the high-angle side. The VO_2 film peaks appear at higher

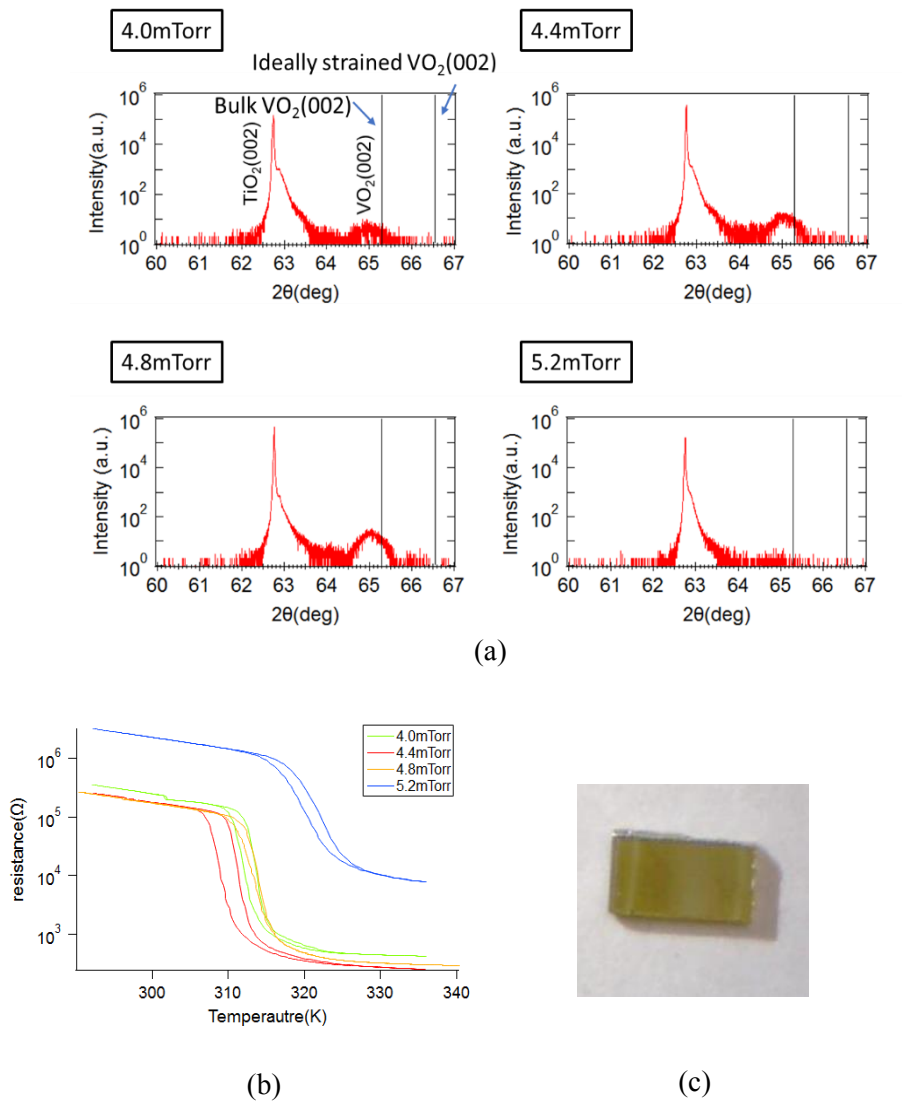


Fig. 5.3: The results of XRD measurement (a) and resistance measurement (b) of VO₂ samples grown at various oxygen pressures. (c) Photo of a sample grown at 4.8 mTorr.

angles, at 65°. Due to the small thickness of the VO₂ film, the VO₂ (002) peaks intensity is much lower than the substrate and the peak width is larger. The *c*-axis lattice parameter of films grown at different oxygen pressures were calculated from the film peak positions, giving 2.870 Å at 4.0 mTorr, 2.865 Å at 4.4 mTorr, and 2.865 Å at 4.8 mTorr. The sample grown at 5.2 mTorr didn't show a clear (002) peak although there is a slight background change at around 64.8°.

The expected position of the bulk VO₂ (002) peak in the XRD pattern is marked with the vertical black lines in Fig. 5.3(a). it is clear that the VO₂ film (002) peak position is close to the bulk VO₂ peak position, which means that the films were fully relaxed

despite the small thickness and no epitaxial strain from the TiO₂ substrate was found. Fig 5.3(b) show the resistance behavior of these four samples. The monoclinic insulating state appears below 310 K in all films and a clear MIT is seen between 310 and 330 K. The measurements were done in 4-point geometry by bonding Al wires directly to the film surface. Since there is some variation in electrode spacings, the plot shows resistance values instead of resistivities, but the variations are generally small. The plots clearly show that the resistance of the sample grown at 5.2 mTorr was much higher than all other films. Considering that this sample did not show a clear XRD diffraction peak, it is reasonable to assign the increase of resistance to a loss of crystallinity or phase. The other three samples showed nearly the same transition properties. For reference, the unstrained bulk VO₂ *c*-axis parameter is 0.2856 Å and the MIT temperature is around 340 K [14].

This oxygen pressure optimization experiment showed that small changes of oxygen pressure do not affect significantly the transport properties as long as the correct VO₂ phase is obtained and the crystallinity is sufficient to produce a clear x-ray diffraction peak. Obviously, other process parameters should be optimized because in these samples the resistive transition is not as sharp as in bulk VO₂ and the MIT temperature is well above the room temperature, which means that the films are not strained.

Fig. 5.4 shows the results of XRD and resistance measurements of samples grown at various temperatures. The oxygen pressure during the deposition was fixed at 4.4 mTorr. The film thickness was the same as before, 20 nm. The laser fluence was 0.56 J/cm² and deposition was done at 2 Hz. The XRD plots show that the VO₂ (002) peak shifted to higher diffraction angles when the deposition temperature was decreased. A higher diffraction angle means that the out-of-plane *c*-axis parameter became smaller, which corresponds to tensile in-plane strain. This is the desired result, since the goal was to fabricate fully strained VO₂ films on TiO₂, which has a slightly larger in-plane lattice parameter than VO₂.

The sample grown at 500 °C showed no VO₂ (002) peak, which suggests that the correct phase was lost. The *c*-axis lattice parameter was calculated as 2.841 Å for 380 °C, 2.859 Å for 410 °C, and 2.865 Å for 440 °C. The smallest *c*-axis lattice parameter was found for the lowest growth temperature of 380 °C, indicating that there is strong tensile strain along the *a* and *b* axes from the TiO₂ substrate, leading to compressive strain along the out-of-plane *c*-axis.

Although the desired strain state was obtained by growth temperature adjustment, the resistance measurement showed that the highly strained film grown at 380 °C has multiple resistive transitions, as plotted in fig. 5.4 (c). The sharp transition at around 300

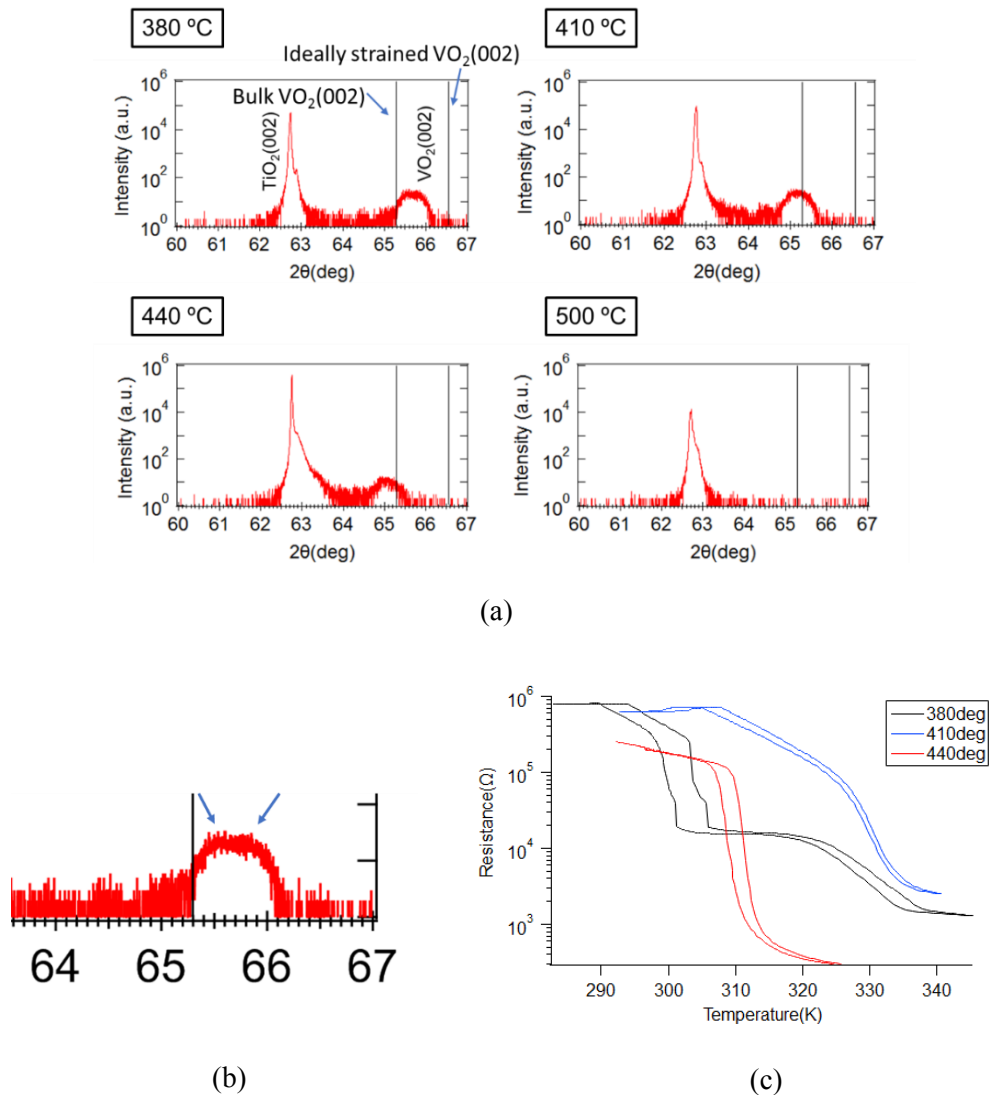


Fig. 5.4 Optimization of growth temperature. (a) XRD results of samples grown at various temperatures. The vertical lines mark the expected positions of fully relaxed and fully strained VO_2 . (b) An enlarged plot of VO_2 (002) peak of the 380 °C sample, showing that the film peak has several components. (c) Results of resistance measurement.

K corresponds to highly strained VO_2 , but the broader transition at around 330 K coincides with unstrained VO_2 . A closer look at the XRD data in fig. 5.4 (b) does indeed show that the film peak consists of multiple components, indicating that this film sample is not homogeneous and two strain states coexist.

To investigate why this strange behavior occurs, thicker and thinner samples were prepared (10 nm and 30 nm thickness). Other deposition conditions were kept the same as for the 380 °C sample. Fig 5.5 shows the results of the XRD and resistance measurements of samples with different thicknesses. The VO_2 (002) peak had the

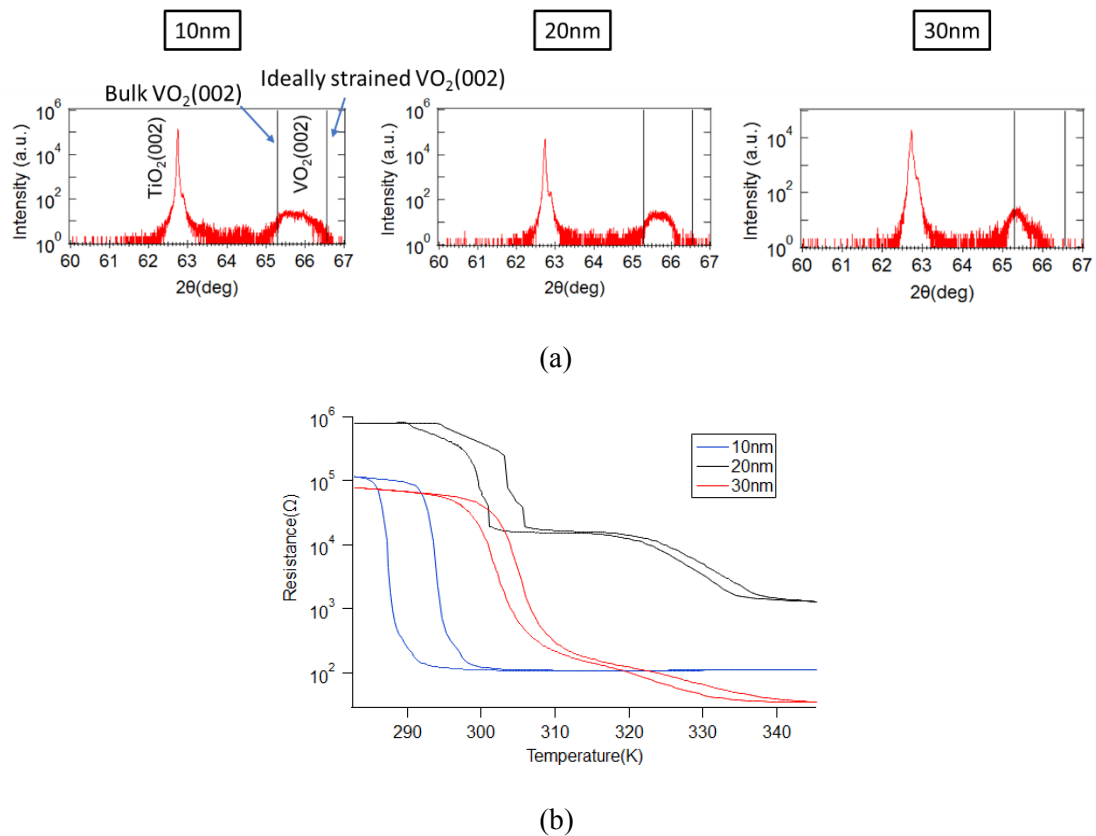


Fig. 5.5 XRD (a) and resistance (b) measurement results of samples with different thicknesses.

largest intensity in the 10 nm thick sample, although the film peak clearly has multiple components. A nearly relaxed part of the peak is close to 65.4° , while a nearly fully strained component is at around 66.2° . The higher-angle component gradually disappears with increasing film thickness and only the relaxed film peak remains for the 30 nm thick sample. Looking at the resistance behavior, only the 10 nm sample showed a single MIT, while the thicker films always showed multiple transitions. From this result, it can be concluded that the strained component dominates the MIT behavior in the 10 nm sample but the influence of the relaxed component increases with film thickness. The critical thickness for strain relaxation is thus between 10 nm and 20 nm.

Fig.5.6 shows models that can be used to understand this MIT behavior. The white area represents the VO_2 film and the blue area corresponds to the TiO_2 substrate. In the 10 nm sample, the film is dominated by the fully-strained part, where the in-plane lattice parameter of the film exactly matches the substrate and the c-axis parameter is smaller. This leads to a single sharp resistance transition and a low transition temperature. In films thicker than 20 nm, some part of the film is relaxed, possibly by generating misfit dislocations. Based on XRD data, it is apparent that these films have both strained and

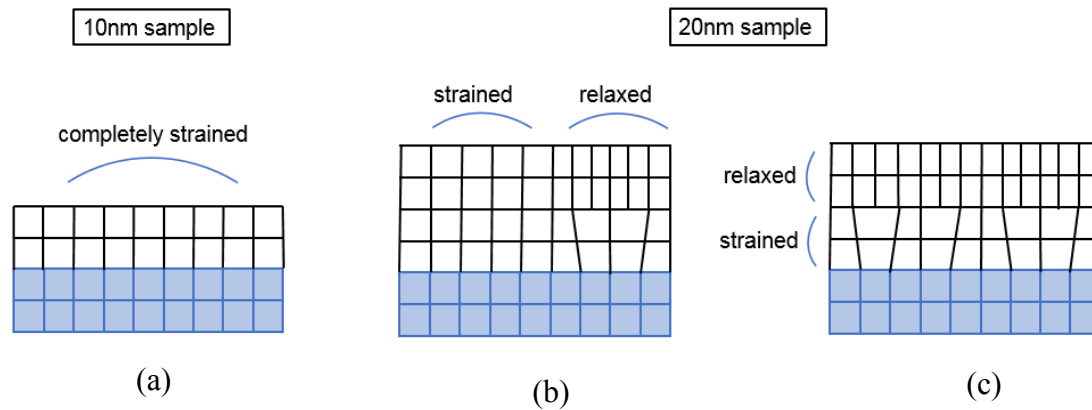


Fig. 5.6 Possible strain relaxation models for thin films that show multiple resistive transitions.

relaxed parts. There are two possible structures that can explain the XRD result. In the structure shown in fig. 5.6(b), some grains maintain the fully strained state while other grains relax. In the model illustrated in fig. 5.6(c), a strained layer exists at the substrate interface while the top part of the film relaxes.

These two models can be distinguished by considering the resistive transition, since the strained and relaxed parts have different MIT temperatures of about 300 K (strained) and 330 K (relaxed). At an intermediate temperature that just exceeds the transition temperature of the strained area, such as 320 K, the relaxed area is still in the insulating state and the resistance of the film measured over a macroscopic distance should still be very high compared to the metallic state. If the temperature increases, the film should show another resistance change at the transition temperature of the relaxed area. On the other hand, in the two-layer structure of fig. 5.6(c), when the temperature exceeds the transition temperature of the strained area, the film resistance should be close to the resistance of the metallic state even if the relaxed surface layer still remains in the insulating state, since the two layers form a parallel circuit. Considering the resistance measurement that show two or even more transitions, it is clear that the model shown in fig. 5.6(b) matches the film structure. This means that different grains in the film have different strain states.

The thickness change experiments show that the 10 nm sample is the best for the purpose of this study because only a single sharp resistive transition occurs close to room temperature. The 10 nm thickness was chosen for later experiments.

Fig. 5.7 shows the results of optimizing the film growth rate, which can be done by changing the ablation laser fluence on the target surface. The film thickness was fixed at 10 nm, the oxygen pressure was 4.4 mTorr, and the growth temperature was 380 °C. The growth rate changes did not cause large differences in the *c*-axis lattice parameter,

which was 2.839 Å at 0.56 J/cm², 2.840 Å at 0.30 and 0.40 J/cm², and 2.835 Å at 0.23 J/cm². Only slight changes were found in the transition temperatures, but samples grown more slowly, at a lower laser fluence showed a sharper transition and higher temperature coefficient of resistance (TCR) which is defined as $\frac{\Delta R}{\Delta T} \frac{1}{R} \times 100$ (%/°C), where R is the film resistance at a reference temperature. Films with a higher TCR are better for use as strain sensors.

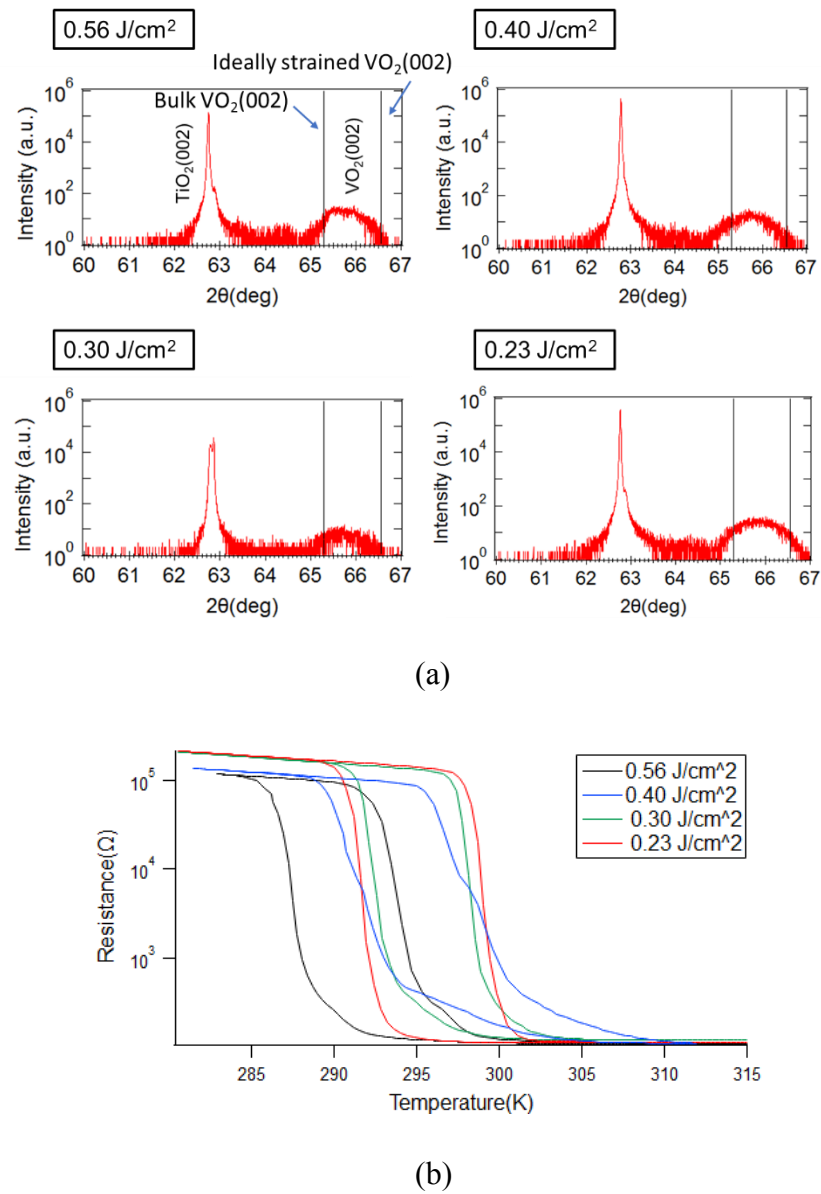


Fig. 5.7 Optimization of laser fluence: (a) The lowest fluence (0.23 J/cm²) gave the largest strain and the sharpest resistance transition (b).

5.2.3 Optical properties of VO₂ thin films

Before performing bending experiments, it was necessary to verify that the VO₂ thin films show an optical reflectance change in the infrared spectral region when crossing the MIT. In this measurement, the MIT was caused by a temperature change controlled by a Peltier device. A schematic view of the measurement setup is shown in fig. 5.8. A thin film sample was placed on a Peltier element that was attached to a copper heat sink. Infrared light reflectivity was measured with a CCD camera. A Xenon lamp was used as a light source, but since the reflectivity change is only visible in the infrared, a 960 nm long-pass filter was used to select strong 980 nm light from the Xe spectrum for measurement. Although the CCD efficiency drops in the infrared, it is still possible to obtain images at the 980 nm illumination. The sample, Peltier device, and a thermistor for temperature control were placed in an Aluminum box that was flushed with dry nitrogen gas to avoid moisture condensation during cooling. A microscope cover glass was used as a window for infrared illumination and camera access. Fig. 5.9 shows an image from the CCD camera. A bare TiO₂ substrate was put next to the sample and used as a reflectivity reference. Images from the CCD camera were collected in a computer and a LabVIEW program was used to integrate the image intensity in two equal-sized regions of interest (ROI), marked with green boxes in fig. 5.9. The average intensity of

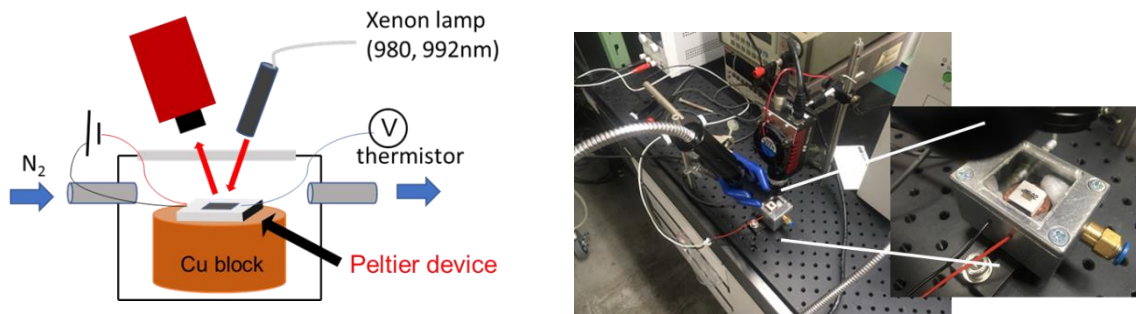


Fig. 5.8 The setup used for film reflectivity measurement.

the VO₂ film ROI was divided by the average obtained from the TiO₂ substrate ROI. This intensity ratio was measured from 280 K to 305 K. A 10 nm VO₂ sample was grown at 4.4 mTorr of oxygen at 380 °C using and a laser fluence of 0.56 J/cm² for this experiment. Fig. 5.10 shows the resistance behavior and the reflected infrared intensity ratio as the temperature was scanned over the MIT. A sharp transition was seen at around 290 K with only a slight secondary transition about 2 K higher.

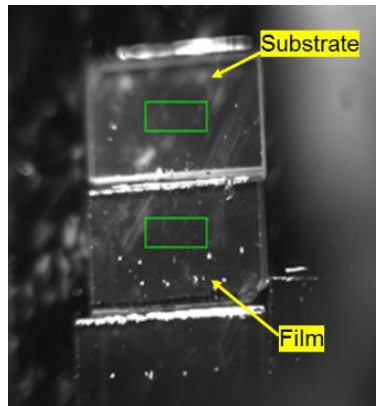
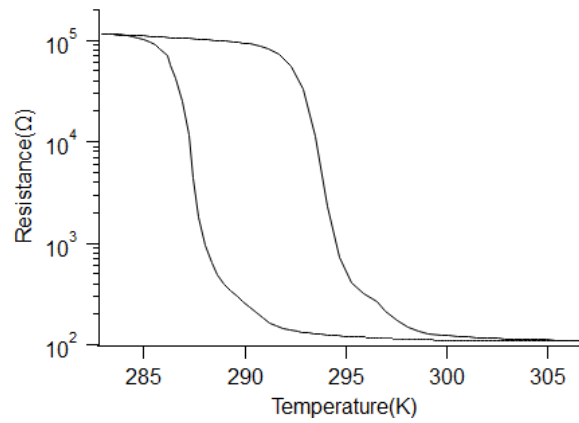
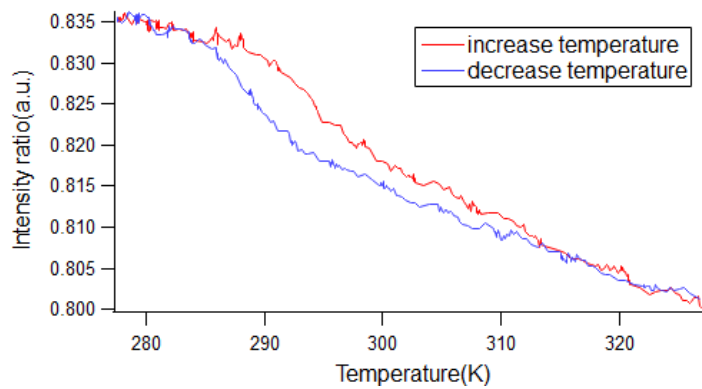


Fig. 5.9 An infrared image of the film sample obtained with a CCD camera. A TiO_2 substrate was placed next to the VO_2 sample for optical reference.



(a)



(b)

Fig. 5.10 Resistance change (a) and reflected light intensity ratio change (b) of a 10 nm VO_2 sample near the MIT.

A reflected light intensity ratio change can be seen during the increase and decrease of temperature near the MIT temperature. When increasing the temperature, a sharp drop occurs at around 295 K, which matches the resistance behavior. Similarly, a sharper change is observed at 290 K in both the reflectivity and resistance datasets. This indicates that as the film state is changing from insulator to metal, the intensity ratio decreases because the metallic area is increasing.

In conclusion, the intensity of reflected light of the VO₂ film is dependent on the state of the film. The reflectivity is higher in the insulating state and lower in the metallic state. The difference in the reflectivity is about 4%. The light seen by the camera is mostly reflected from the polished back of the substrate. The reflectivity drop in the metallic state is thus related to an increase of free-carrier absorption in the film in the metallic state. The film is more transparent in the insulating state and thus the intensity of light reflected from the back of the substrate is higher. The camera-based reflectivity analysis is thus mostly measuring a change in the film transmission coefficient.

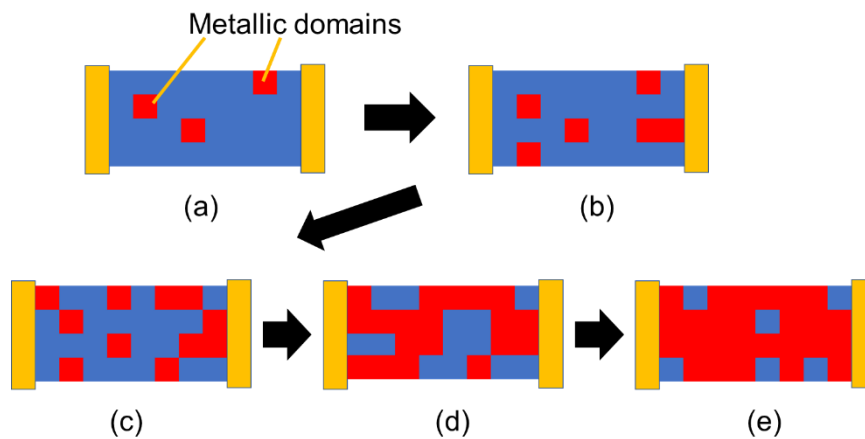


Fig. 5.11 Illustration of domain structures during MIT. Red area shows the metallic domains and blue area corresponds to insulating domains.

While both resistance and reflectance show a sharp drop during MIT, the magnitude of this decrease is different. This behavior can be understood by looking at Fig. 5.11, which shows a schematic illustration of the domain structure close to the MIT temperature. Fig. 5.11 (a) illustrates the insulating state at a temperature slightly below the T_c, while (e) illustrates the metallic state at a slightly higher temperature than the T_c. When increasing temperature, micro- or nanoscale domains switch independently from an insulating to the metallic state and the ratio of metallic domains increases. Spatially separated but coexisting metallic and insulating domains can be observed optically. The relationship between the conductivity change and the fraction of the metallic domains

can be explained by percolation theory. The conductivity σ during percolation behavior can be shown as

$$\begin{aligned}\sigma(P) &= \sigma(P-P_c)^t \quad (P > P_c) \\ \sigma(P) &= \text{constant} \quad (P < P_c)\end{aligned}$$

where P is the fraction of the metallic domains and $1 - P$ is that of the insulating domains at a certain temperature. P_c , the critical fraction, is the fraction of metallic phases when the metallic domains connect between the two electrodes. T is the critical exponent. If there is no connecting path between the metallic domains, conductivity does not change when the temperature increases, although the ratio of metallic domains increases. However, when a conducting path forms between the metallic domains, connecting two electrodes, the resistance suddenly drops. This causes a resistance change of several orders of magnitude over a temperature range of just a few degrees. On the other hand, the optical reflectivity change is more gradual, even at temperatures where P is lower than P_c . Therefore, the reflectance gradually decreases along with the gradual increase of the fraction of metallic domains and the reflectance does not show as sharp change as the percolative resistance transition.

5.3 Bending stage and measurement system

5.3.1 Thinner substrate for bending

The in-plane strain applied on a thin film in a three-point bending geometry depends on the substrate crystal thickness. Since the film thickness is just 10 nm, it is clear that the stiffness and crack failure of the substrate limits the maximum strain that can be applied on the film since the usual commercial oxide substrates are 0.5 mm thick. It is therefore better to use a softer substrate, but since the substrate material is fixed, the only free parameter is the substrate thickness. The only commercially available choice is thus a 0.2 mm-thick TiO_2 substrate.

HF wet-etched and annealed substrates are available from Shinkosha. The actual picture and structural properties of the substrate are shown in fig. 5.12. This etched and annealed surface is different from the polished substrates used earlier. The surface is very flat, although a step and terrace structure is not clearly visible. Since the MIT temperature and sharpness of a VO_2 film is very sensitive to the substrate surface microstructure, additional optimization of growth conditions was required. Fig. 5.13

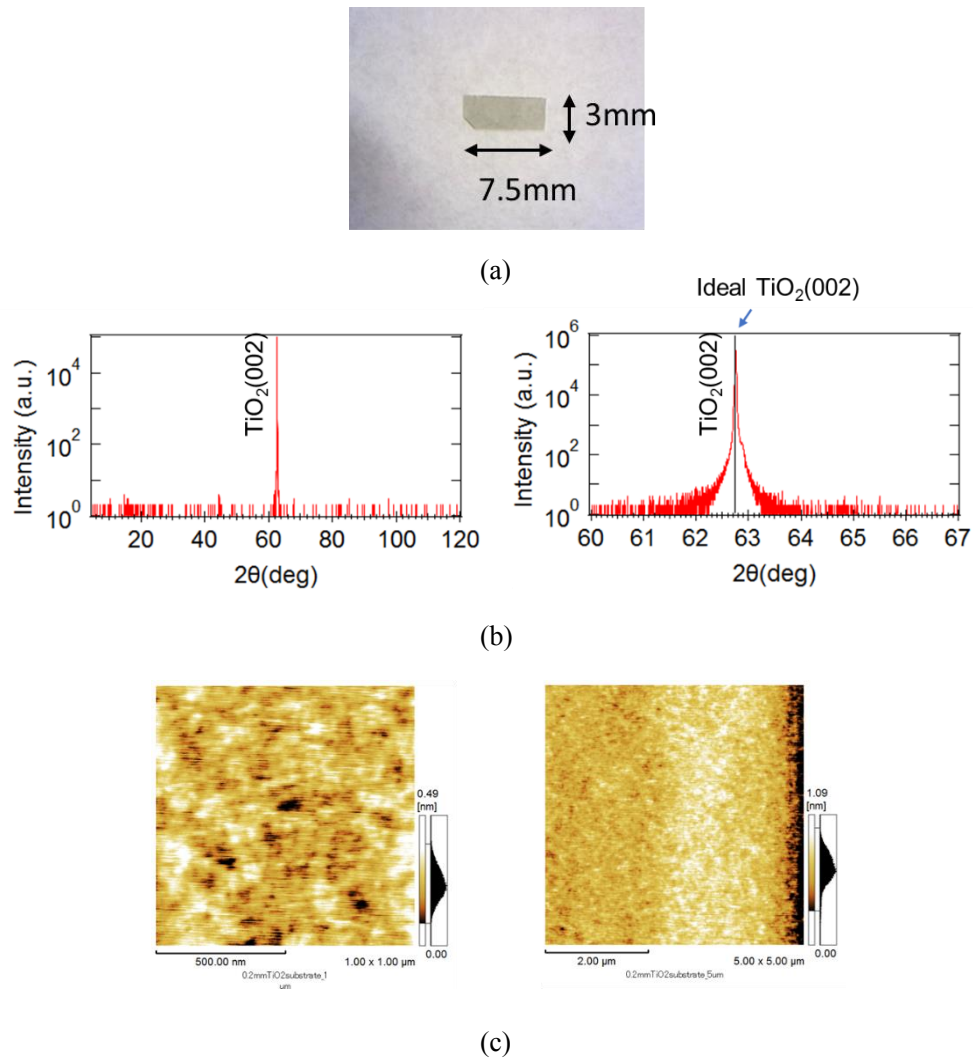
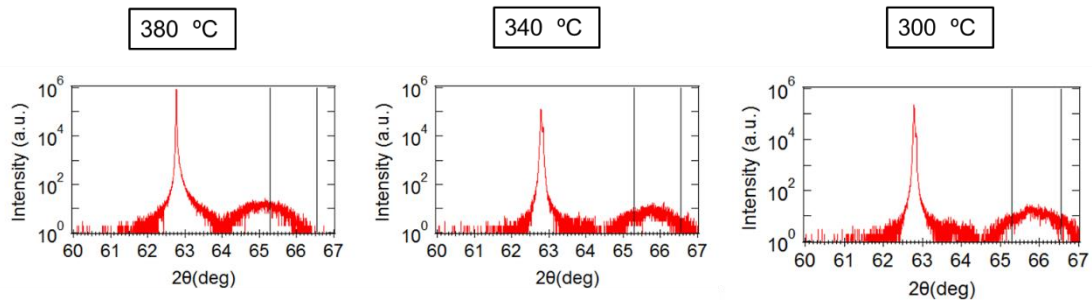


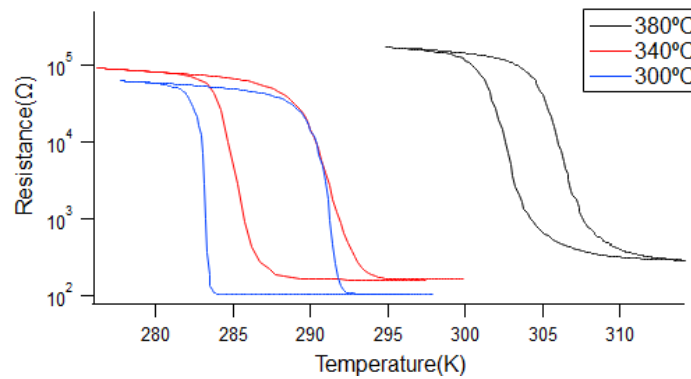
Fig. 5.12 A picture of a 0.2 mm thick TiO_2 substrate (a), reference XRD scans (b), and AFM images of the as-received surface (c).

shows the results of the optimization of growth temperature. The film thickness was 10 nm to obtain a fully strained film. The ablation laser fluence and pulse rate were 0.56 J/cm^2 and 2 Hz. The background oxygen pressure was 4.4 mTorr. When the VO_2 film was deposited on a thin substrate at the same conditions as was used for the 0.5 mm substrates, the transition temperature shifted about 10 degrees higher, from 295 K to 305 K. Based on the XRD measurement, it was apparent that the sample grown at 380°C was not highly strained because the VO_2 (002) peak was close to the bulk VO_2 position at around 65.2° . A strained film was obtained by decreasing the growth temperature further, down to 300°C , shifting the VO_2 (002) peak to higher diffraction angle, close to 66° and the transition temperature also shifted lower, indicating the increase of strain from the substrate. Based on literature the observed difference in optimal growth

conditions on differently prepared substrate surfaces is reasonable. As shown in fig. 5.13, the surface conditions of a substrate have a large influence on the transport properties of VO₂ films. Finally, the sample grown at 300 °C was used for bending measurement because the transition was very sharp and the transition temperature was close to room temperature.



(a)



(b)

Fig. 5.13 Optimization of growth temperature for wet-etched substrates. (a) The *c*-axis lattice parameter calculated from the XRD patterns was 2.863 Å (380 °C), 2.838 Å (340 °C), and 2.833 Å (300 °C). (b) Resistive transitions for each growth temperature.

5.3.2 Reference for film reflectance measurement

To measure small reflectance changes that are caused by the VO₂ film and to eliminate any possible influence from the substrate or effects related to camera temperature drift or light intensity changes, a reference is needed. To eliminate such problems, reflected light intensity from a thin film sample can be compared with light intensity reflected from a bare TiO₂ substrate. In experiments described in Chapter 5.2.3, two different samples were placed side-by-side in the measurement cell. However, a separate sample cannot be used in the bending experiment because it is impossible to bend two crystals exactly the same way and it is thus impossible to guarantee that any observed light intensity change is caused purely by a MIT in the VO₂ film. One simple way to solve this problem is to grow a film on just one half of a substrate. In this way, the shape of the bare substrate part of the sample and the film part are almost the same during bending, so substrate effect can be eliminated by dividing the reflection intensity from the film by the intensity of light reflected from the substrate. Since the PLD chamber is designed with internal stencil masks, this modification did not require any deposition hardware changes. Fig. 5.14 (a) shows monitor images taken with a camera directly in front of the sample (at a viewport at the bottom of the PLD chamber). The images show an uncovered sample crystal on a sample holder and the positioning of an edge mask that covers half of the sample surface. A photograph of a VO₂ film sample prepared in this way is shown in fig.5.14 (b). There was no film in the upper part of the substrate, which is very slightly lighter. The VO₂ film was deposited only on the lower half of the substrate and this part has a pale yellow tint. This sample was used in actual bending measurements.

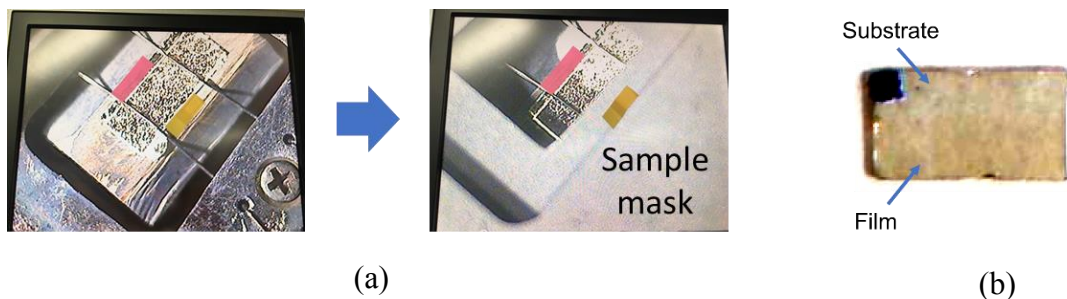


Fig. 5.14 The sample picture in the chamber before masking and with a mask covering half of the crystal (a). Photo of the sample after deposition (b).

5.3.3 The bending stage and the measurement system

A bending stage was made to measure various properties (resistance, reflectance, shape of the sample) while bending the sample by applying force using a piezo actuator [30]. Fig. 5. 15 shows the design of the bending stage. An aluminum block was used as a frame. Two Peltier devices (CP0.8-31-06L, Laird Technologies) were glued to the front surface of the aluminum frame with silver epoxy. The two Peltier elements provide uniform temperature control and can either cool or heat the sample by about 30 degrees relative to room temperature. Aluminum was used as the frame material because of good thermal conductivity to carry away heat from the Peltier elements and because aluminum is easy to machine. The Peltier devices work as heat pumps and can thus be used to either heat or cool the sample simply by changing the polarity of the drive current.

The sample crystal was attached to a thin (0.1 mm) copper sheet with black SEM tape. The tape served two functions. Since the tape is conducting, it provides reasonably good thermal contact while also reducing stray light reflections. It is thus easier to measure the intensity of light reflected from the thin film sample. A thin film thermistor (103FT1005A, SEMTEC) was glued with silver epoxy close to the sample on the copper sheet for temperature monitoring and for PID temperature control. The

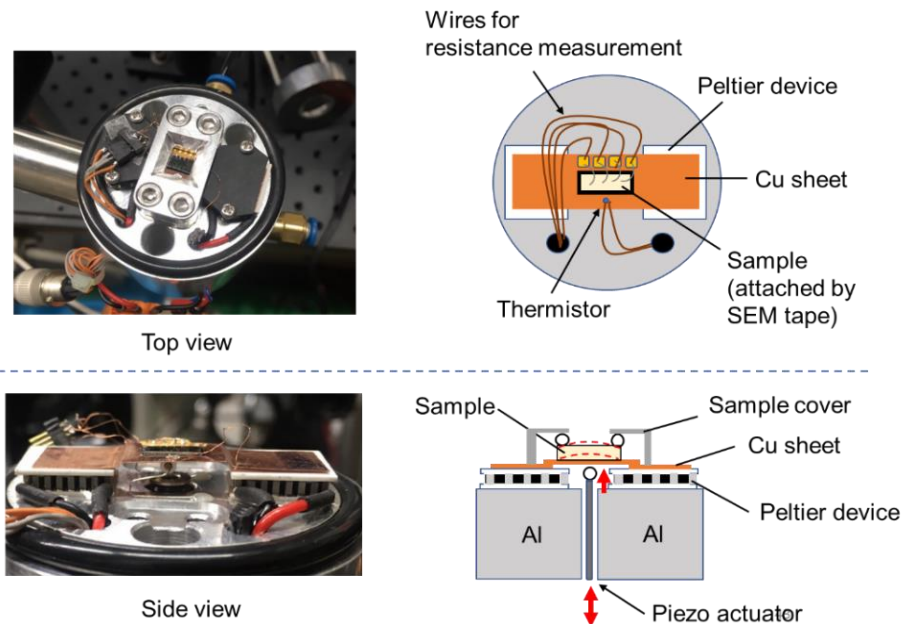


Fig. 5.15 Actual pictures (left) and schematic diagram (right) of the bending stage.

temperatures reported here refer to this measured copper sheet temperature. There may thus be a slight temperature difference between the reported temperature and the true surface temperature of the sample. However, since in these measurements, the actual temperature is not important, as long as the temperature is fixed in the middle of the metal-insulator transition, no further attempt was made to calibrate this temperature difference. The copper sheet was then clamped with plastic pressure clamps onto the Peltier elements. Copper was chosen as the carrier metal because it is a good heat conductor and mechanically soft.

Sample resistance was measured by four-probe method at the same time with the reflectance measurement. An electrode sheet was glued to the copper sheet next to the sample crystal. Ultrasonic wire bonding was used to attach four 20 μm bonding wires between the sample surface and the electrode pads. Thicker copper wires were soldered to the electrode pads and a miniature pin header connector was used to make connections to the feedthrough cables. The connector can be seen on top of the left-hand Peltier device in the top view photograph in fig. 5.15.

The sample was fixed by an aluminum sample cover (top view photo). Alumina pipes (1 mm diameter) were glued onto the aluminum cover to provide well-defined pressure points on the edges of the substrate crystal. The alumina pipes also provided the necessary heat insulation of the sample surface from the aluminum frame. The sample can be bent when another 2-mm diameter alumina cylinder pushes the bottom of the sample with a piezo actuator. The piezo actuator was set at a position just close to the copper sheet with a manual micrometer set screw mounted on a spring-loaded pre-tension stage at the back of the aluminum frame.

The stage sample area and all mechanics were enclosed with air-tight caps and dry nitrogen gas was flushed through the stage during measurement to prevent water condensation during sample cooling. All wires and mechanical feedthroughs were made air tight by epoxy gluing or by O-ring seals. An optical window made from a microscope slide cover glass was glued to the sample space cover for optical access.

Fig. 5.16 shows geometry of the measurement system and the associate optics. A fiber-coupled focus lens of a Xe lamp was placed at the top, at an angle of about 30° from the sample normal to illuminate the sample with near-infrared light. The Xe lamp was filtered with a band-pass filter that selected the strong 980 and 992 nm peaks of a Xe lamp. The reflected infrared light was monitored with a CCD camera that was filtered with a 975 nm long-pass filter, eliminating the ambient room light. Since the fluorescent lamps in the room have essentially no near-infrared emission, this setup allowed normal room lighting to be used during the measurement. The camera images

were acquired with a LabVIEW program for reflectivity analysis.

From left side, a 635 nm diode laser was mounted on a beam expander to provide homogeneous illumination with a parallel beam over the whole sample surface. The reflected laser light was passed through a cube beam splitter, which was selected to avoid laser interference fringes that appeared when a simple glass plate beam splitter was used. One beam path (center of fig. 5.16) had a Shack-Hartmann wavefront sensor, which measure the shape of the spatial variation of the wavefront of a light beam. Since the incident laser light passed through a beam expander producing a parallel beam, the initial wavefront was flat. When this light beam reflects from a curved sample surface, the optical wavefront is deformed. This deformation is measured with the Hartmann wavefront sensor, which provides a real-time image of the curved reflecting surface. The advantage of this sensing technique is that it provides a three-dimensional image of

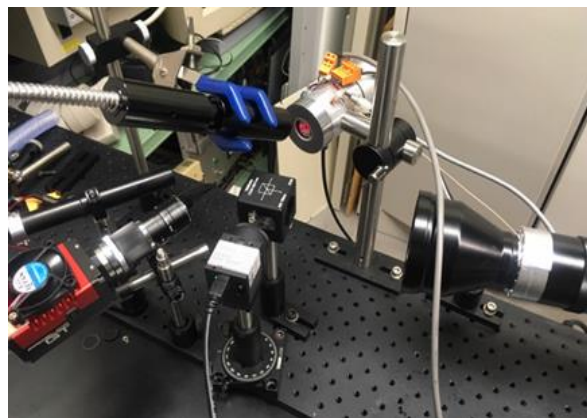
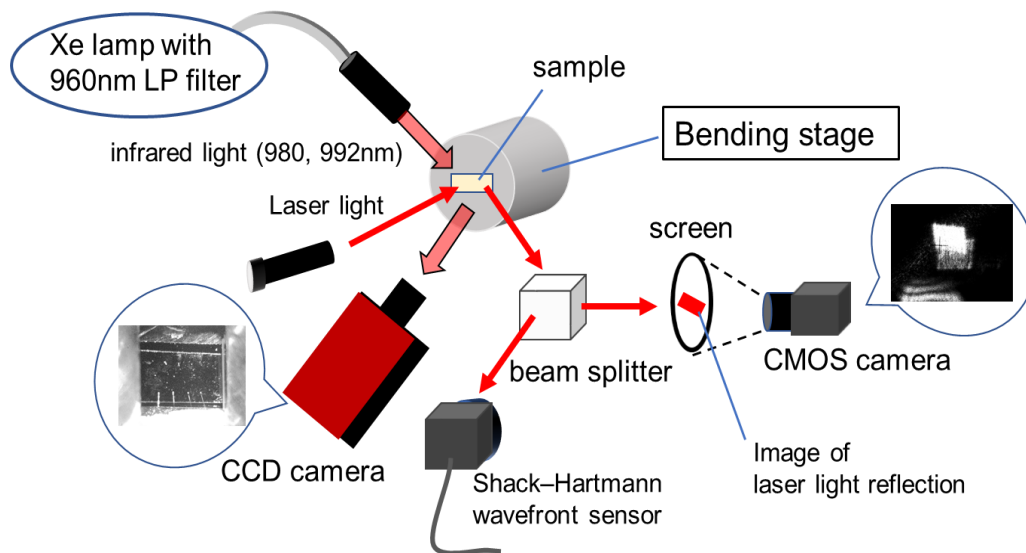


Fig. 5.16 Geometry of the measurement system.

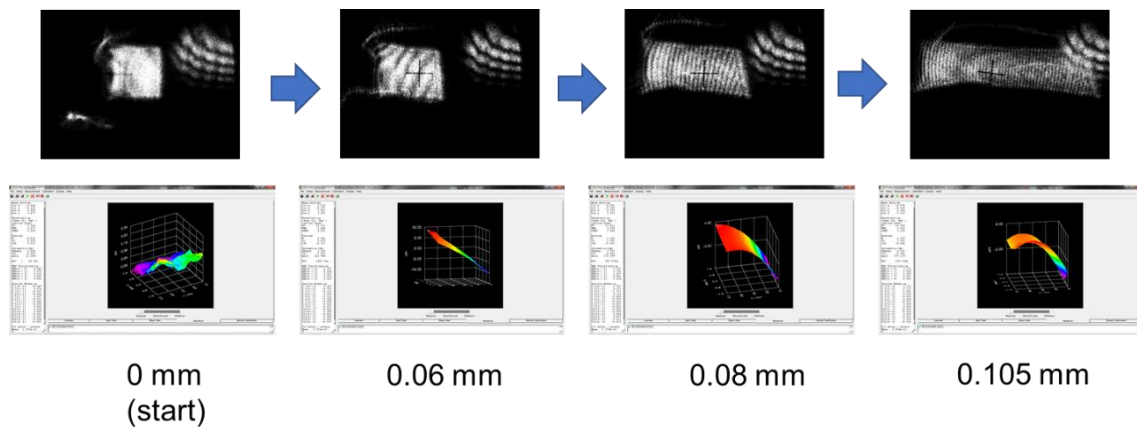


Fig. 5.17 The reflection image and corresponding wavefront shape during the bending of a Si substrate. At the start, the pressure cylinder just touched the backside of the substrate without deforming it. The substrate broke when the cylinder pushed the substrate by about 100 μm .

the whole crystal surface, even when the bending is nonuniform or there is a torsional deformation component. The Hartmann camera images were acquired with special software to reconstruct the wavefront image and to perform real-time model fitting to obtain a quantitative cylindrical curvature values while the crystal is deformed.

The other beam from the beam splitter was directed at an etched glass diffusive screen that was mounted on another digital CCD camera. This image can be observed visually and gives direct information on the bending angles of the sample surface. As shown in fig. 5.17, the reflected image is initially square but become broader when the crystal is bent. The sample shape during bending was calculated by performing constant edge search in LabVIEW and determining the width of the reflected sample image. Fig. 5.17 shows the change of the reflection image on the screen and corresponding wavefront shape. In this measurement, a Si substrate was put on the sample stage instead of a TiO_2 sample because Si is relatively soft compared to TiO_2 and easier to bend to larger angles. The substrate was pushed with the manual micrometer screw until the substrate cracked.

Fig.5.18 shows a LabVIEW program which was used in this measurement. Two camera images are monitored on the left side. Two parameters (width of reflection image and curvature) for the shape of bending sample are shown in the middle of right three panels. The reflected image width is measured automatically from the image. The wavefront curvature data is obtained from another computer that runs the Hartmann camera fitting software. The merit of this wavefront analyzer is that it shows the actual surface shape in real time while adjusting the sample stage as shown in fig. 5.19.

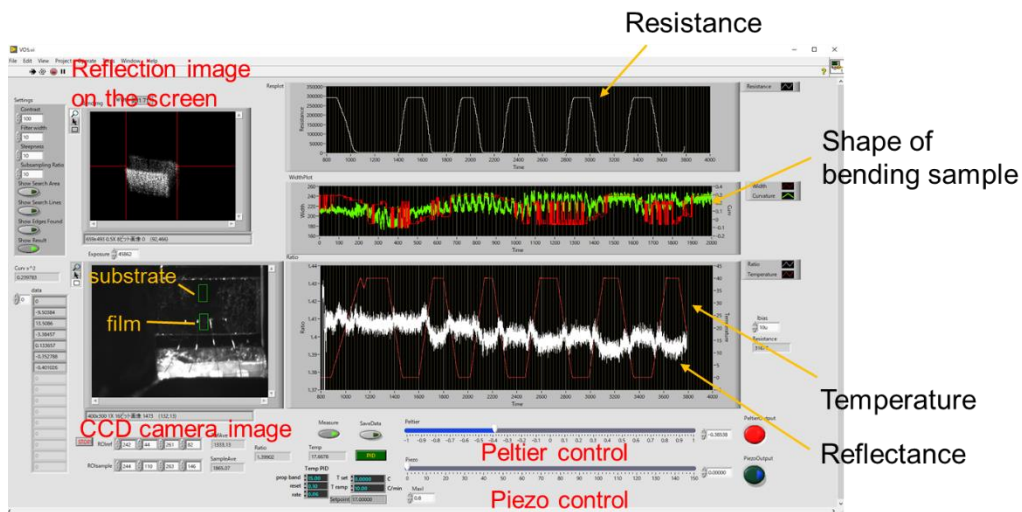


Fig. 5.18 LabVIEW program for monitoring and controlling measurement parameters.

The sample resistance is shown at the right top panel while temperature and reflectance ratio are shown in right bottom pane. This reflectance ratio is equal to the average intensity of the film reflection divided by the average intensity of the substrate reflection. The averaging area is marked with green boxes in the left-hand near-infrared camera image. The sample temperature and the piezo actuator length can be controlled by changing the current of the Peltier device and the voltage of the piezo actuator.

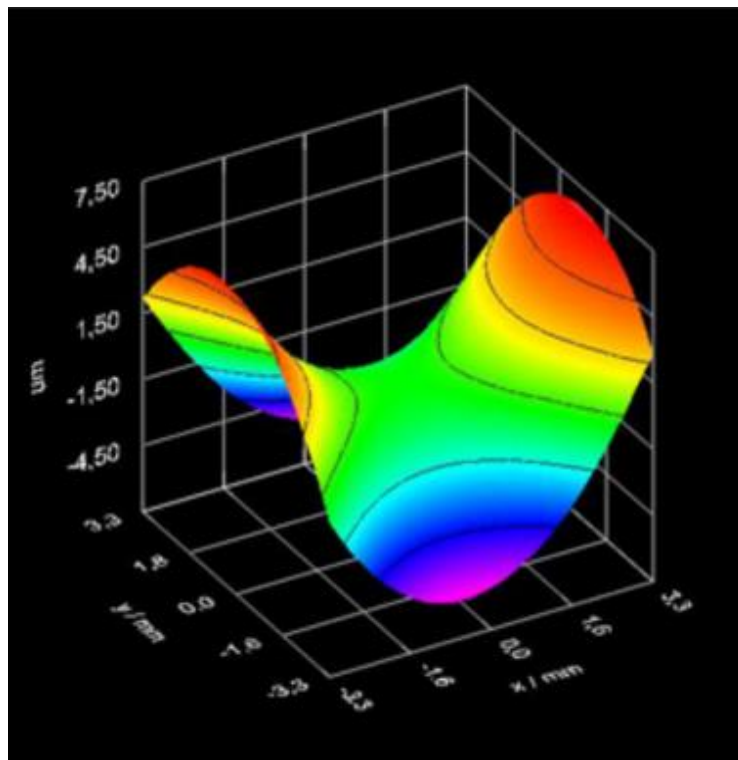


Fig. 5.19 An example of wavefront image. [33]

5.4 Strain dependent optical reflectivity of VO₂ thin films

5.4.1 Calculation of strain value

Fig. 5.20 shows a diagram of a sample before and after deformation. $\varepsilon(x)$ is the position-dependent sample deformation, where the x -axis runs parallel to the length of the substrate and $\varepsilon(x)$ measures the distance in the vertical direction. Strain is applied to the substrate at the center from the bottom as shown in fig. 5.20. In this case, $\varepsilon(x)$ can be represented as

$$\varepsilon(x) = \frac{Fx^2(3L-2|x|)}{8Yt^3y} . \quad (5.1)$$

In this equation, F is the bending force at the center, t is the sample thickness, L is the sample length, Y is the Young's modulus of TiO₂, and y is the width of the substrate. $\varepsilon(L/2)$ is the crystal displacement between the center and the edge, and it can be calculated from Eq. 5.1 as

$$\frac{\varepsilon(x)}{\varepsilon(L/2)} = \frac{2x^2(3L-2|x|)}{L^3} . \quad (5.2)$$

The in-plane strain, δ_{ab} , is a function of the distance from the center position of the sample in the x direction. However, the film thickness is much smaller than the substrate thickness so it is possible to assume that δ_{ab} is always the same as the strain at the substrate surface. In this case, δ_{ab} can be represented as

$$\delta_{ab} = \frac{t}{2R(x)} = \frac{t}{2} \left\{ \frac{1}{[1+\varepsilon'(x)^2]^{3/2}} \frac{d^2\varepsilon}{dx^2} \right\} \sim \frac{t}{2} \frac{d^2\varepsilon}{dx^2} = \frac{12t\varepsilon(L/2)}{L^3} \left(\frac{L}{2} - |x| \right) . \quad (5.3)$$

where $R(x)$ is the curvature radius and $\varepsilon(x)$ is assumed to be very small. Therefore, δ_c can be calculated as

$$\delta_c = -0.3892 \delta_{ab} . \quad (5.4)$$

where the Poisson ratio was obtained from literature [29].

The resistance was measured at the center part at a distance about 2.2 mm, so strain was calculated at the position where $x = 0.55$ mm while $L = 5.45$ mm, which is the distance between the ceramic spacers. It was assumed that δ_{ab} and δ_c are constant in the measurement area, so δ_c can be calculated from Eqs. 5.3 and 5.4 as

$$\begin{aligned} \delta_c &= -0.3892 \delta_{ab} \sim -0.3892 \left\{ \frac{12t \varepsilon(5.45/2)}{5.45^3} \left(\frac{5.45}{2} - |0.55| \right) \right\} \\ &= -6.3 \times 10^6 \times t \varepsilon(L/2) \% \end{aligned} \quad (5.5)$$

If t and $\varepsilon(L/2)$ are known, δ_c can be calculated.

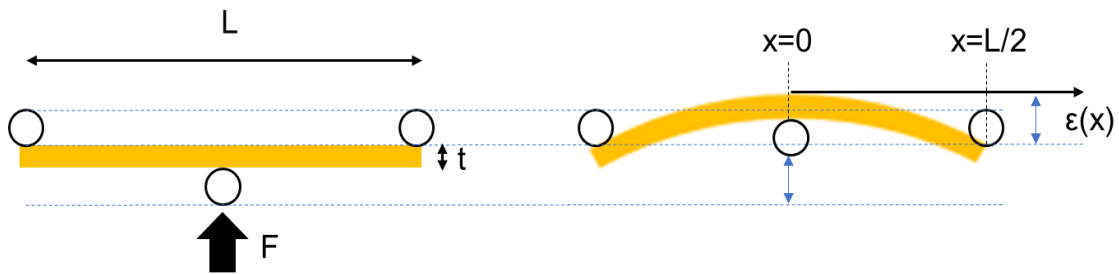


Fig. 5.20 A diagram of the substrate before and after deformation and definition of parameters.

5.4.2 Resistance measurement on the bending stage

The resistance of the sample that was prepared as described in Chapter. 5.4 was measured on the bending stage. When inducing the MIT by bending the film, the temperature should be stable to remove the contribution of temperature to the MIT. The temperature also should be in the middle of the transition temperature range because the sensitivity of the film to other outside stimuli, such as light or strain is the highest. Fig. 5.21 shows the resistance behavior of the sample on the bending stage. In this time the sample was not deformed and this MIT was caused by controlling the temperature. From this result, 15 °C was chosen as the temperature for the bending experiments because it is at about the middle point between the metal and insulator states during decreasing temperature.

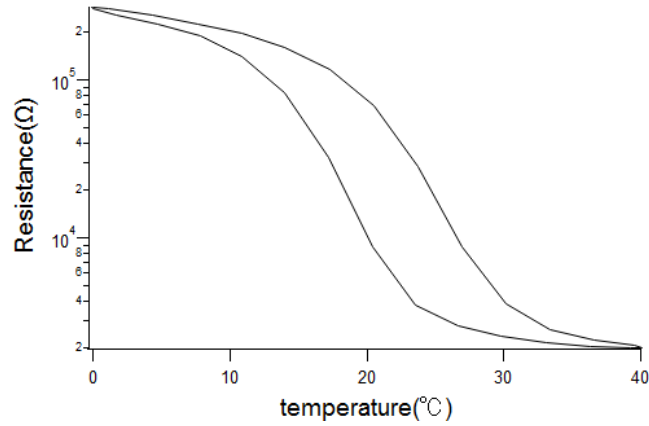


Fig. 5.21 The resistance behavior of a VO₂ film sample measured on the bending stage.

5.4.3 MIT properties during sample bending

After fixing the sample temperature at 15 °C, the sample was pushed with the piezo actuator while measuring the reflectance, resistance, and the sample shape. A constant voltage was applied to the actuator for several tens of seconds and a number of data points were acquired for later averaging. The voltage applied to the actuator was gradually increased from 10 V to 40 V in 10 V steps. The sample was allowed to recover the initial state between each measurement by setting the piezo actuator voltage to zero for about a minute. The width of reflection image was changing when voltage

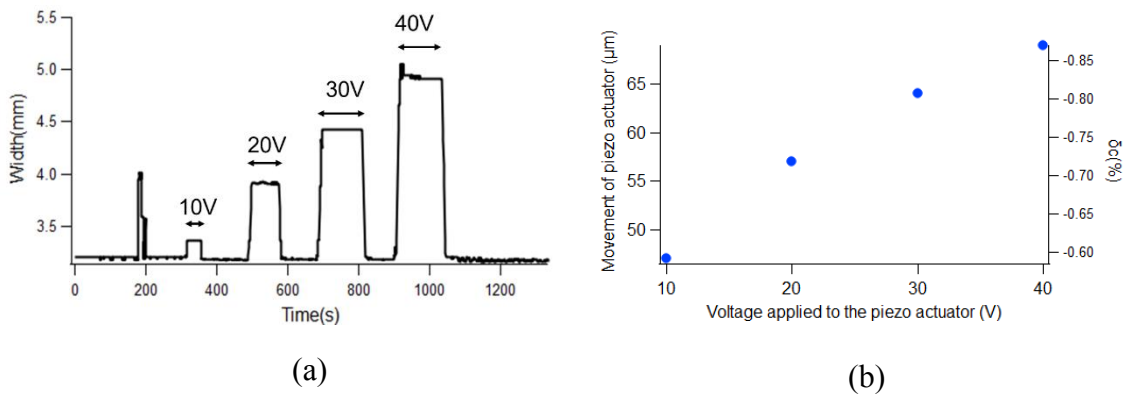
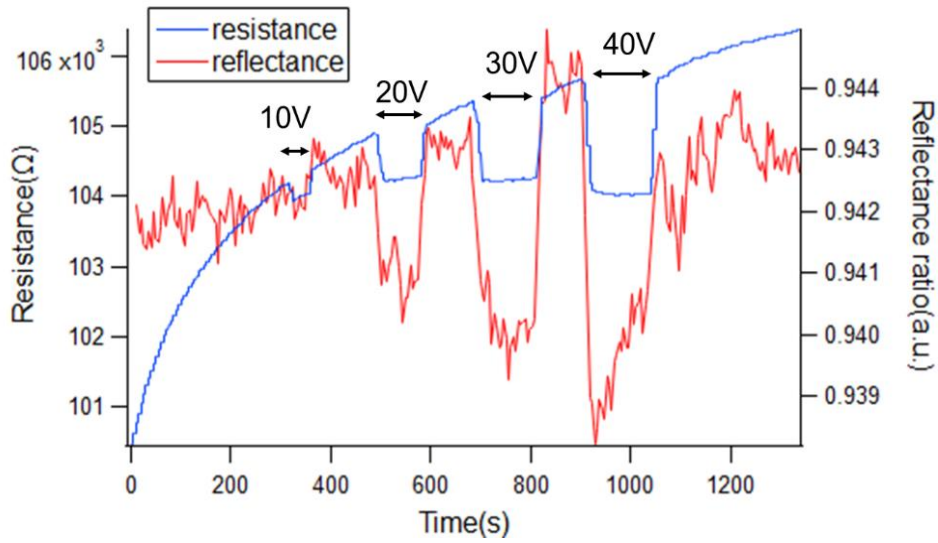


Fig. 5.22 (a) Measured reflection image width as a function of the applied piezo actuator voltage and (b) displacement of the actuator from the original position (left axis) and calibrated δ_c (right axis).

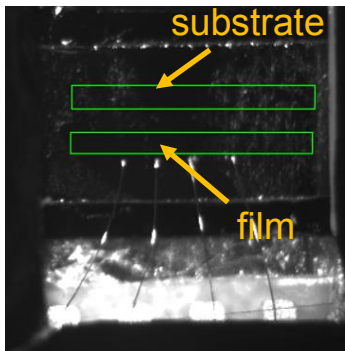
was applied to the piezo actuator as shown in fig. 5.22 (a). The image width was clearly proportional to the applied piezo voltage. From this result and the result shown in fig.5.17, the displacement caused by the applied voltage was compared to the known displacement generated with a micrometer screw. The calibration factor for the piezo displacement vs. applied voltage could thus be calculated as shown in fig. 5.22 (b). This displacement is equal to $\epsilon(L/2)$. By substituting this $\epsilon(L/2)$ and t , which is 0.2 mm in this measurement in Eq. 5.5, the value of δ_c was estimated as shown in fig. 5.22 (b). The maximum value of δ_c that could be obtained before the sample cracked was about -0.87 %. The sign of the strain indicates that the out-of-plane strain was compressive while the sample was stretched in the in-plane direction by the bending.

Fig. 5.23 (a) shows the resistance and reflectance changes measured while the sample was being deformed. The blue line indicates the resistance of the film and the red line indicates the reflectance ratio of reflection intensity. The black arrows mark the periods when a voltage was applied to the actuator. When voltage was applied to the piezo actuator, applying bending strain on the sample, the resistance dropped suddenly and recovered again when the bending force was released. This resistance drops became larger as the applied voltage and thus the applied bending force was increased. The sample temperature was set close the midpoint of the resistive MIT transition. At this temperature, the sample contains a mixture of both metallic and insulating domains. The drop of resistance observed when strain was applied on the sample indicates that a larger proportion of the VO₂ film converted from an insulating to a metallic state. The resistance change of VO₂ films close to the MIT is percolative, which means that individual grains in the film change the phase at slightly different temperatures. Under constant temperature, the conversion may be induced by mechanical strain. It is clear from the measurement that applying higher strain converted a larger proportion of grains to metallic state. As was explained in chapter 5.2.2, there is correlation between transition temperature and the c -axis lattice parameter. If the crystal has a shorter c -axis lattice parameter due to compressive strain applied along the c axis, the MIT shifts to lower temperatures. Therefore, when compressive out-of-plane (c -axis) strain is applied by bending, the transition temperature shifts to lower temperature, and a larger part of the film shifts to the metallic state. This change of the ratio of metallic and insulating grains or domains in the film is seen in the resistance measurement.

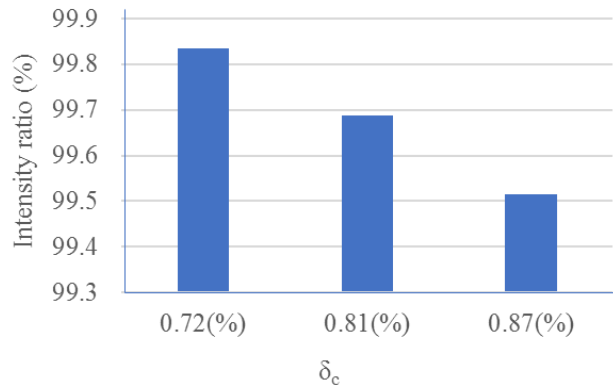
At the same time, as the resistance drops, the reflectance ratio also shows a sudden drop for each applied voltage and the magnitude of this drop is also proportional to the magnitude of the bending. Due to the limitations of the Si CCD camera, the measurements were done at around 900 nm where the reflectivity change between the



(a)



(b)



(c)

Fig. 5.23 (a) Resistance (left axis) and reflectance (right axis) of the sample when the sample was bending. (b) Measurement area of reflectance. (c) Drops of intensity ratio of reflection as a function of the δ_c .

metallic and insulating states is quite small. Due to that, there is considerable noise in the measured reflectance ratio and small change are difficult to detect reliably, especially for low applied strain (for example, 10 V). Fig. 5.23 (b) shows the actual CCD image, marking the regions of interest where the reflectance was measured for the film and substrate parts of the sample. The averaging area is wider than for the resistance measurement. It was assumed that increasing the averaging area would help to reduce noise levels due to greater averaging. Therefore the δ_c , which was calculated for the center part of the sample, where the resistance was measured, the average δ_c in the optical averaging area would be slightly smaller, since δ_c is a function of distance from the sample center. The reflection intensity ratio was averaged by acquiring many

images over a period of a few tens of seconds before and after bending. The result is shown in fig. 5.23 (c). The reflectance ratio dropped by about 0.5% when a *c*-axis strain of 0.87% was applied. The intensity drop became larger as a function of δ_c .

The magnitude of this intensity change during the MIT caused by bending is not very different from a temperature scan over the MIT, which gave a reflectance change of about 4.2% as shown in fig. 5.10, even though the magnitude of the resistance change is very small during bending (about 1%) compared to a temperature scan across the MIT (about three orders of magnitude). This difference is caused by the domain structure and percolative conduction of the VO₂ film during the MIT. When increasing the temperature close to the MIT, the sample is originally in the insulating state below the MIT. As the temperature increases, some metallic domains form and the number of metallic domains or the size of the domains increase as a function of temperature. Initially, while these metallic domains are surrounded by insulating parts of the film, there is very little change in the film resistance. The resistance drops suddenly when a percolative transition occurs and a metallic path forms between metallic domains, connecting the electrodes used for resistance measurement. On the other hand, the reflectance signal is proportional to the area ratio of metallic and insulating domains regardless of whether the metallic domains are electrically connected or not, which means that the reflection intensity drop is much more gradual in the MIT region than the resistive transition.

In conclusion, proper functioning of the bending stage and the measurement system was successfully confirmed. As shown here, a decrease of the reflection intensity of a VO₂ film as a function of strain can be measured optically with a simple CCD camera setup.

6. Conclusion

This study focuses on the strain effects in oxide thin films. The first purpose of this study was to fabricate free-standing BaTiO₃ piezoelectric films on flexible support for vibration energy harvesting device. High-quality BaTiO₃ thin film cannot be grown on flexible support, so transfer process of BaTiO₃ thin film need to be developed. BaTiO₃/BaO / SrTiO₃ heterostructures were fabricated for the transfer process. From XRD measurement, epitaxial BaTiO₃ thin film was grown on BaO layer. By attaching this sample to glass substrate and by etching only BaO layer, SrTiO₃ substrate was removed and thus BaTiO₃ thin film could be transferred to another substrate successfully.

The second purpose of this study was to measure the local strain of thin films on flexible substrate by using the optical reflectance change of VO₂ film during metal-insulator transition (MIT) which is caused by strain. For this purpose, VO₂ thin films with sharp MIT was fabricated and characterized. Resistance behavior was corresponding to the c-lattice parameter. In detail, a sample having longer c-lattice parameter (relaxed VO₂ film) shows gradual transition at higher temperature, while a sample having shorter c-lattice parameter (strained VO₂ film) shows sharp transition at lower temperature. It is considered that structural transformation by the strain from the substrate caused this transition behavior change. Using the highly strained sample having sharp transition, optical reflectance measurement was done. The intensity of reflection of infrared light was changed along with the resistance change in a temperature range of 10 °C to 50 °C. When increasing the temperature, the reflectance was decreasing with the decrease of resistance. It is considered that the absorbance of VO₂ thin films increase at high temperature. To use this optical property as a strain sensor of thin films, a new measurement setup was developed for applying uniaxial strain on a thin film sample by bending the substrate. Resistance and reflectance were measured while applying the strain to the VO₂ sample having sharp transition at around 15 °C. The strain level was increased by applying higher voltages to the piezo actuator. The resistance and reflectance decreased under static strain and the amount of change was proportional to the magnitude of the strain in both of resistance and reflectance. Since the MIT temperature is strain dependent, when measuring resistance or reflectivity at a fixed temperature, any additional bending strain will further shift the MIT, and thus an additional fraction of the sample will switch from insulating to metallic state, decreasing resistance and reflectance. This result that compressive strain along c-axis induce the MIT shift to metal state, is corresponding to the fact that

compressive strain along c-axis from the substrate also induce MIT shift to metal state.

Therefore, near-infrared reflectance of a VO₂ thin film is determined by the internal strain and can thus be used as an internal strain sensor for spatial strain mapping in flexible devices.

References

- [1] J. V. Zalk, P. Behrens, *Energy Policy* 123, 83 (2018).
- [2] Y. Wand, H. He, R. Xu, *ADV MECH ENG* 7, 1 (2015).
- [3] P. Ovartchaiyapong, K. W. Lee, B. A. Myers, A. C. B. Jayich, *Nat. Commun* 5, 4429 (2014).
- [4] H. Tanaka, H. Takami, T. Kanki, A. N. Hattori, K. Fujiwara, *J. Appl. Phys* 53, 05FA10 (2014).
- [5] S. E. Park, T. R. Shrout, *IEEE Transactions on Ultrasonics, Ferroelectrics, and Frequency Control* 44, 1140 (1997).
- [6] K. Uchino, *Acta Mater* 46, 3745 (1998).
- [7] Q. M. Wang, Q. M. Zhang, B. M. Xu, R. B. Liu, *J. Appl. Phys* 86, 3352 (1999).
- [8] J. B. Ihn, F. K. Chang, *Smart Mater* 13, 609 (2004).
- [9] X. D. Wang, J. Zhou, J. H. Song, J. Liu, N. S. Xu, Z. L. Wang, *Nano Lett* 6, 2768 (2006).
- [10] H. S. Kim, J. H. Kim, J. A. Kim, *Int. J. Precis. Eng. Man* 12, 1129 (2011).
- [11] R. Calio, U. B. Rongala, D. Camboni, M. Milazzo, C. Stefanini, G. Petris, M. Oddo, *Sensors* 14, 4755 (2014).
- [12] M. G. Kang, W. S. Jung, C. Y. Kang, S. J. Yoon, *Actuators* 5, 1 (2016)
- [13] H. Wei, H. Wang, Y. Xia, D. Cui, Y. Shi, M. Dong, C. Liu, T. Ding, J. Zhang, Y. Ma, N. Wang, Z. Wang, Y. Sun, R. Wei, Z. Guo, *J. Mater. Chem* 6, 12446 (2018).
- [14] C. Kim, Y. Oikawa, J. S. Shin, H. Ozaki, *J. Phys. Condens. Matter* 18, 9863 (2006).

- [15] V. Eyer, ANN. Phys. (Leipzig) 11, 650 (2002).
- [16] Y. Muaroka, Z. Hiroi, APL 80, 583 (2002).
- [17] Y. Muraoka, Y. Ueda, Z. Hiroi, J. Phys. Chem. Sol 63, 965 (2002).
- [18] H. Liu, S. Lysenko, A. Rua, V. Vikhnin, G. Zhang, O. Vasquez, F. E. Fernandez, J. Luminescence 119-120, 404 (2006).
- [19] S. Lysenko, A. J. Rua, V. Vikhnin, J. Jimenez, F. Fernandez, H. Liu, Appl. Sur. Sci 252, 5512 (2006).
- [20] V. S. Vikhnin, S. Lysenko, A. J. Rua, F. Fernandez, H. Liu, Optical Materials 29, 1385 (2007).
- [21] M. Nakajima, N. Takubo, Z. Hiroi, Y. Ueda, T. Suemoto, APL 92, 011907 (2008).
- [22] J. Sakai, M. Kurisu, PRB 78, 033106 (2008).
- [23] K. Nagashima, T. Yanagida, H. Tanaka, T. Kawai, J. Appl. Phys. 101, 026103 (2007).
- [24] K. Kawatani, H. Takami, T. Kanki, H. Tanaka, Appl. Phys. Lett 100, 173112 (2012).
- [25] H. Kakiuchida, P. Jin, S. Nakao, M. Tazawa, Jpn. J. Appl. Phys 46, L113 (2007).
- [26] S. Hasegawa, Char, Mater (2012).
- [27] N. Cerniglia, P. Wang, J. Electrochem. Soc 109, 508 (1962).
- [28] C. Merckling, G. Saint-Girons, C. Botella, G. Hollinger, M. Heyns, J. Dekoster, M. Caymax, Appl. Phys. Lett 98, 092901 (2011).
- [29] K. Nagashima, T. Yanagida, H. Tanaka, T. Kawai, Phys Rev B 74, 172106 (2006).

[30] T. Kikuzuki, M. Lippmaa, *Appl. Phys. Lett* 96, 132107 (2010).

[31] M. M. Qazilbash, M. Brehm, B. G. Chae, P.-C. Ho, G. O. Andreev, B. J. Kim, S. J. Yun, A. V. Balatsky, M. B. Maple, F. Keilmann, H. T. Kim, D. N. Basov, *Science* 318, 1750 (2007).

[32] Y. Muraoka, Z. Hiroi, *Appl. Phys. Lett* 80, 583 (2001).

[33] https://www.thorlabs.com/newgrouppage9.cfm?objectgroup_id=5287/.

Acknowledgments

I have many people to thank for helping my study in these two years. I would like to express my gratitude to them here.

Foremost, I would like to express my sincere gratitude to Professor Mikk Lippmaa for polite guidance and kind support in my mater period. I was learned from him not only the basic knowledge of oxide thin films and experiments technique, but also how to solve the problem in the experiments and how to develop new instruments, and so on. I have learned a lot of things from him and I will make use of these experiences in my life.

I am also grateful to Dr. Ryota Takahashi. He always gave me many valuable advices in these two years. I was taught from him about the basic technique of experiments including making films, and how to proceed the experiments.

I would like to thank to laboratory member. I thank Dr Jiyeon Lee for giving many advices about not only study but also life in master's course. Mr. Katsuya Kihara and Mr. Yoshihisa Hosokawa helped me very much during job hunting. I also appreciate Mr. Tatsuya Kikuzuki for the previous study he have done. Without his study, I couldn't take on this study.

I would like to thank to Ms. Junko Kawamura and Ms. Junko Nagayama. They always kindly helped me for administrative work.

Finally, I would like to express my deep gratitude to all my friends in ISSP for their kind support and encouragement in my life in Kashiwa.

January 2019

Ogawa Kodai